Characterizing Quantum Instruments: From Nondemolition Measurements to Quantum Error Correction

Roman Stricker,[1,*] Davide Vodola,[2,3] Alexander Erhard,[1] Lukas Postler,[1] Michael Meth,[1] Martin Ringbauer,[1] Philipp Schindler,[1] Rainer Blatt,[1,4,5] Markus Müller,[6,7] and Thomas Monz[1,5]

[1] *Institut für Experimentalphysik, Universität Innsbruck, Technikerstr. 25, Innsbruck A-6020, Austria*

[2] *Dipartimento di Fisica e Astronomia, Università di Bologna, Bologna I-40129, Italy*

[3] *INFN, Sezione di Bologna, Bologna I-40127, Italy*

[4] *Institut für Quantenoptik und Quanteninformation, Österreichische Akademie der Wissenschaften, Otto-Hittmair-Platz 1, Innsbruck A-6020, Austria*

[5] *Alpine Quantum Technologies GmbH, Innsbruck 6020, Austria*

[6] *Institute for Quantum Information, RWTH Aachen University, Aachen D-52056, Germany*

[7] *Peter Grünberg Institute, Theoretical Nanoelectronics, Forschungszentrum Jülich, Jülich D-52425, Germany*

(Received 22 October 2021; accepted 13 July 2022; published 3 August 2022)

In advanced quantum processors, quantum operations are increasingly processed along multiple in-sequence measurements that result in classical data and affect the rest of the computation. Because of the information gain of classical measurements, nonunitary dynamical processes can affect the system, which common quantum channel descriptions fail to describe faithfully. Quantum measurements are correctly treated by so-called quantum instruments, capturing both classical outputs and postmeasurement quantum states. Here we present a general recipe for characterizing quantum instruments and demonstrate its experimental implementation and analysis. Thereby the full dynamics of a quantum instrument can be captured, exhibiting details of the quantum dynamics that would be overlooked with standard techniques. For illustration, we apply our characterization technique to a quantum instrument used for the detection of qubit loss and leakage, which was recently implemented as a building block in a quantum error-correction (QEC) experiment [Nature 585, 207 (2020)]. Our analysis reveals unexpected and in-depth information about the failure modes of the implementation of the quantum instrument. We then numerically study the implications of these experimental failure modes on QEC performance, when the instrument is employed as a building block in QEC protocols on a logical qubit. Our results highlight the importance of careful characterization and modeling of failure modes in quantum instruments, as compared to simplistic hardware-agnostic phenomenological noise models, which fail to predict the undesired behavior of faulty quantum instruments. The presented methods and results are directly applicable to generic quantum instruments and will be beneficial to many complex and high-precision applications.

DOI: 10.1103/PRXQuantum.3.030318

The field of quantum computation progresses rapidly and experiments demonstrate ever more complex tasks. The majority of experiments have focused on a unitary evolution of quantum systems together with a single final measurement. In modern systems, the time evolution of a computation may get repetitively interrupted by in-sequence measurements and circuit adaptation conditional on the result. These measurements are required for many classes of semiclassical algorithms, including quantum error correction (QEC) [1–7], resource-efficient Fourier transform [8,9], and measurement-based quantum computing [10]. Owing to its destructive nature, a quantum measurement produces classical data and changes the quantum state in a nonunitary fashion. Operations including such in-sequence measurements therefore deviate from simple linear unitary evolution and can no longer be described with commonly used methods. For prime examples such as QEC codes or quantum nondemolition (QND) measurements [11–17], it is important to keep track of the measurement outcome in each experimental cycle. More subtly, experimental imperfections in realizations of quantum operations are often caused by undesired coupling to

*Corresponding author. roman.stricker@uibk.ac.at

other quantum systems [18–24]. As a consequence, the operations that are performed on what is considered a qubit usually feature a small nonunitary component due to coupling to and ignorance of other relevant degrees of freedom. Such small deviations often go unnoticed when enforcing a unitary description onto the system [19].

The correct framework to describe such quantum classical operations is given by so-called *quantum instruments* [25,26]. A quantum instrument includes both quantum and classical inputs as well as outputs and thereby offers a unified description of state preparation, operations, and quantum measurements [27]. Quantum instruments are commonly used to describe scenarios where one needs to keep track of a classical input or output of a quantum operation, e.g., in the description of quantum networks [28], quantum causality [29], measurement uncertainty trade-offs [30,31], and weak measurements [32–34].

So far, device-independent [35] and self-testing [36,37] protocols have been developed to assess the performance of positive operator-valued measures [38,39] and quantum instruments. However, these methods do not give full information on the dynamics that is required in the context of present high-precision quantum computation [40–46] and QEC.

Here, we present a characterization method for quantum instruments that will be particularly useful to characterize building blocks of quantum information processors. We identify quantum instruments where conventional quantum process tomography fails and introduce relaxed tomography procedures beyond the underlying computational subspace (e.g., qubit levels), suitable for completely reconstructing such quantum instruments. We contrast instrument reconstruction to conventional quantum process tomography that typically applies some form of maximum likelihood estimation (MLE) and demonstrate those to bear the risk of unfaithful reconstruction potentially incorporating nonphysical results. This becomes particularly crucial in high-performance applications. Our detailed experimental analysis is guided by a very general example of a QND measurement dedicated to the detection of qubit loss and leakage featuring in our recent work [11] and conveys processes that can drastically deteriorate the performance of QEC codes, if these loss mechanisms go unnoticed [47–49]. These findings apply to generic QND measurements just as well, featuring, for example, in leakage studies beyond trapped ions [50], real-time stabilizer measurements [51,52] for QEC or in metrology applications [53].

Based on an experimental quantum instrument reconstruction using a modified process tomography scheme, we derive a full instrument description for a faulty QND loss detection unit. We numerically study its effect on a QEC cycle on a low-distance near-term logical qubit. This instrument tomography proves to be particularly useful for assessing the QEC performance, since it allows us to evaluate the effects of different microscopic processes in the loss detection and to estimate the parameter regimes where QEC becomes beneficial. Importantly, those detailed noise dynamics are only accessible upon full instrument reconstruction, while remaining mostly hidden to conventional process tomography. Although the parameters of the precise modeling remain implementation specific, its results reveal general scaling properties, such as the impact of false-positive and false-negative events on error correcting code performances. Those properties together with our tool and its workflow apply to other architectures just as well.

Our results further highlight the importance of developing microscopic, experimentally informed noise models of faulty quantum instruments over widely used generic hardware-agnostic noise models such as dephasing or depolarizing noise channels.

The methods we develop provide the tools and theoretical framework to reconstruct and characterize quantum instruments, such as QND measurements, which have a prominent role in all quantum computing architectures even beyond QEC, as, for instance, in quantum information and quantum metrology [54].

I. INTRODUCTION TO QUANTUM INSTRUMENTS

Formally, a quantum instrument $\mathcal{I}$ is a set I of trace nonincreasing, completely positive (CP) maps $\{\mathcal{E}_j\}_{j\in I}$, labeled by an index $j \in I$, with the property that their sum is trace preserving (TP), $\mathrm{Tr}(\sum_j \mathcal{E}_j(\rho)) = \mathrm{Tr}(\rho)$ for every state ρ; see Fig. 1. For example, when $\mathcal{I}$ describes a quantum measurement, then $j \in I$ labels the measurement outcomes and $\mathcal{E}_j$ transforms the input state ρ to the eigenstate corresponding to outcome j. In this case, each $\mathcal{E}_j$ will generally be trace decreasing, while the sum of all $\mathcal{E}_j$ will be trace preserving for any orthonormal measurement basis. Performing, for example, a computational basis measurement via an ancilla defines two CP maps $\mathcal{E}_0 = |0\rangle\langle 0|$ and $\mathcal{E}_1 = |1\rangle\langle 1|$. Both are trace decreasing (except for computational basis states), since they measure the overlap between ρ and the computational basis states, but their sum must be trace preserving as they form a complete basis and the measured probabilities must add up to 1.

The quantum instrument for a measurement $\mathcal{I}\colon \mathcal{H}_1 \mapsto \mathcal{H}_2 \otimes \mathbb{C}^{|I|}$ thus maps the input Hilbert space $\mathcal{H}_1$ to an output Hilbert space $\mathcal{H}_2$ of potentially different size, and a classical space $\mathbb{C}^{|I|}$. In practice, one might realize such a measurement by coupling the system to an ancilla and subsequently measuring the ancilla with a set of orthogonal projectors $|j\rangle\langle j| \in \mathbb{C}^{|I|}$; see Fig. 1. This final ancilla measurement extracts the classical measurement outcome j, which identifies which operation $\mathcal{E}_j$ was applied to the system. In the following we focus on the simplest case with two possible measurement outcomes ($|I| = 2$), but

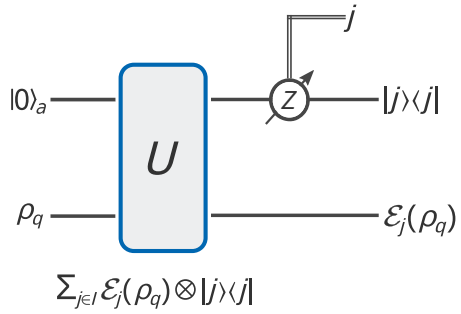

FIG. 1. Example of a quantum instrument. The operation U realizes a generic quantum instrument on the system in initial state ρ_q and writes index j of the applied operation into the state of an ancilla initialized in state $|0\rangle_a$. The ancilla is finally projected onto the computational basis to read out the classical index.

all results can be straightforwardly extended to the general case.

II. TOMOGRAPHY OF QUANTUM INSTRUMENTS

For qubit systems, complete information on their quantum evolution can be gained by quantum process tomography [55]. However, when the evolution is described by a quantum instrument, the constituent maps are, in general, not individually trace preserving. For example, if leakage from the qubit level is present, the tomographic measurements do not probe the full Hilbert space. In this case standard reconstruction techniques such as maximum likelihood estimation [56,57] will not be able to describe the quantum dynamics faithfully, because they force the reconstructed map to be trace preserving. To approach this problem, we rely on a relaxed tomography algorithm that does not enforce trace preservation [19,58,59].

In order to reconstruct the quantum channel $\mathcal{E}$, we make use of the Choi-Jamiolkowsky (CJ) isomorphism [60] to relate $\mathcal{E}$ to an (unnormalized) map Λ, the *Choi operator*. The correspondence between Λ and $\mathcal{E}$ is given by

$$\mathcal{E}(\rho) = \mathrm{Tr}_1[(\rho^T \otimes \mathbb{1})\Lambda].$$

The Choi operator Λ with respect to the basis $\{|k\rangle\}_{k=0}^{d-1}$ can be explicitly constructed as

$$\Lambda = \sum_{k,l}^{d-1} |k\rangle\langle l| \otimes \mathcal{E}(|k\rangle\langle l|),$$

where d is the dimension of the Hilbert space. Following the notation of Ref. [19], the probability $p_{i,j}$ for observing outcome state ρ_j after preparing state ρ_i and subjecting it to the non-trace-preserving channel described by the Choi operator Λ is given by

$$\begin{aligned} p_{ij} &= \mathrm{Tr}[\rho_j^\dagger \mathrm{Tr}_1[(\rho_i^T \otimes \mathbb{1})\Lambda]] \\ &= \mathrm{Tr}[(\rho_i^T \otimes \rho_j^\dagger)\Lambda]. \end{aligned} \tag{1}$$

Defining the projector $\Pi_{ij} \equiv \rho_i^* \otimes \rho_j$ with ρ_i and ρ_j representing pure states alongside the column vector $|\Lambda\rangle\!\rangle = \sum_{i,j}^{d-1} \Lambda_{i,j} |j\rangle \otimes |i\rangle$, obtained by stacking the columns of Λ (similarly for $|\Pi_{ij}\rangle\!\rangle$), we can identify the trace in Eq. (1) with an inner product of the vectorized operators:

$$p_{ij} = \langle\!\langle \Pi_{ij} | \Lambda \rangle\!\rangle. \tag{2}$$

We now define the vector of observed frequencies $|f\rangle$, and the quadratic form S, as

$$|f\rangle = \sum_{i,j} f_{ij} |i,j\rangle,$$
$$S = \sum_{i,j} |i,j\rangle\langle\!\langle \Pi_{ij}|.$$

The most direct way to reconstruct the non-trace-preserving Choi operator Λ is by inverting the above relation, a technique known as *linear inversion*,

$$\hat{\Lambda} = \arg\min_\Lambda \| S|\Lambda\rangle\!\rangle - |f\rangle \|_2, \tag{3}$$

where $\|\cdot\|_2$ denotes the vector 2-norm, and the estimator $\hat{\Lambda}$ is analytically given by

$$\hat{\Lambda} = \sum_{i,j} p_{ij} \left(\sum_{l,m} |\Pi_{lm}\rangle\!\rangle\langle\!\langle \Pi_{lm}| \right)^{-1} |\Pi_{ij}\rangle\!\rangle.$$

Unfortunately, linear inversion can produce nonphysical results, especially in situations where the true (Choi) state is close to pure [56]. To avoid these problems, we can use modified maximum likelihood estimation by constraining the estimator to be positive semidefinite, i.e., a physical state:

$$\begin{aligned} &\text{minimize} \quad \| WS|\Lambda\rangle\!\rangle - W|f\rangle \|_2 \\ &\text{subject to} \quad \Lambda \geq 0. \end{aligned} \tag{4}$$

Here $W = \sum_{i,j} \sqrt{N_j / p_j (1-p_j)} |i,j\rangle\langle i,j|$ is a weight matrix, taking into account the multinomial distribution of observed frequencies. Note that in contrast to standard MLE quantum process tomography [61], i.e.,

$$\begin{aligned} &\text{minimize} \quad \| WS|\Lambda\rangle\!\rangle - W|f\rangle \|_2 \\ &\text{subject to} \quad \Lambda \geq 0, \mathrm{Tr}[\Lambda] = d, \end{aligned} \tag{5}$$

we do not enforce the map to be trace preserving in Eq. (4).

III. EXPERIMENTAL SETUP

The experimental demonstrations are realized on a string of $^{40}Ca^{+}$ ions confined in a linear Paul trap in ultrahigh vacuum [62]; see Fig. 2(a). Each ion represents a physical qubit encoded in the metastable electronic states $S_{1/2}(m = -1/2) \equiv |0\rangle$ and $D_{5/2}(m = -1/2) \equiv |1\rangle$, denoting the computational subspace. Upon coherent laser-ion interaction, we realize a universal set of quantum gate operations combining single-qubit rotations by an angle θ around the x or y axis of the Bloch sphere, $R^{\sigma_j}(\theta) = \exp(-i\theta\sigma_j/2)$ with the Pauli operators $\sigma_j = X_j$ or Y_j acting on qubit j, together with two-qubit Mølmer-Sørenson entangling gate operations $R^{\mathrm{MS}}_{i,j}(\theta) = \exp(-i\theta X_i X_j/2)$ [63]. Multiple addressed laser beams allow for arbitrary two-qubit connectivity across the entire ion string [64]. Readout is performed through continuous excitation of a dipole transition, solely involving the lower S-state and collecting its scattered photons, which identifies the qubit's $|0\rangle$ and $|1\rangle$ states. This dipole laser collectively covers the entire ion string. However, we are also able to read out only a subset of the qubit register by shelving electronic populations of certain qubits in the upper D-state manifold, referred to as *addressed readout*. This constitutes an essential building block for realizing the in-sequence detections featuring in QND measurements. Beyond the qubit level, we hold equivalent control over the entire S- and D-state Zeeman manifolds, which allows us to encode a higher-dimensional quantum decimal digit (qudit) in each ion. Implementing our example quantum instrument requires us to take the additional level $D_{5/2}(m = +1/2) \equiv |2\rangle$ into account—forming together with the qubit states a qutrit. A qutrit readout demands for two subsequent measurements to separate both D-state levels, namely $D_{5/2}(m = -1/2) = |1\rangle$ and $D_{5/2}(m = +1/2) = |2\rangle$. Because each measurement scatters photons and heats up the ion string, we counteract every in-sequence measurement with polarization gradient cooling, keeping the quality of postmeasurement gate operations high.

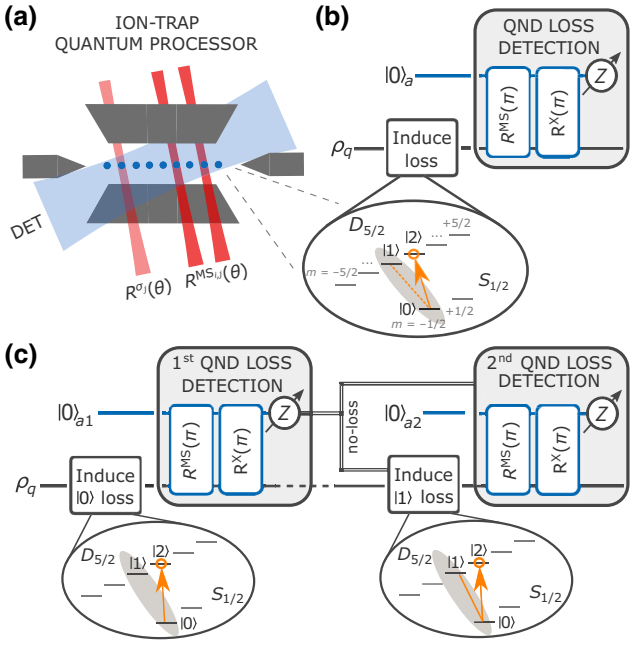

FIG. 2. Ion-trap quantum processor and qubit loss detection unit as the example quantum instrument. (a) Schematic of our ion-trap quantum processor, where each ion resides along a linear string representing a single qubit. Quantum gate operations are realized upon coherent laser-ion interaction using tightly focused beams addressing single ions for local gates (bright red) and a pair of ions for entangling gates (dark red). Readout is performed via collective fluorescence detection (DET). See the text for details. (b) A QND qubit loss detection unit as our application example for a quantum instrument. The system qubit is encoded in the computational subspace $\{|0\rangle_q, |1\rangle_q\}$ and is affected by loss to a third level $|2\rangle_q$. For details, see the text. (c) A quantum erasure channel implemented by first inducing partial loss from $|0\rangle_q$ followed by its detection using the gadget from (b). Conditional on the qubit not being lost, the same partial loss is induced from $|1\rangle_q$ and subsequently detected.

IV. EXAMPLE: QUBIT LOSS DETECTION

We experimentally study an example quantum instrument devised for a QND detection of qubit loss or leakage, which represents a key building block towards fault-tolerant quantum computation. Qubit loss occurs in a variety of physical incarnations such as the actual loss of particles encoding the qubits or chemical reactions that make qubits unutilizable. Those mechanisms occur almost never on experimental timescales as particles can be stably trapped for days and working in ultrahigh vacuum prevents chemical reactions. However, the implementation of quantum computational tasks can often be improved by addressing higher-dimensional states, either to spectroscopically decouple certain constituents (e.g., qubits) from subtasks or to improve the quantum circuit. Furthermore, faulty state initialization bears the risk of leakage to levels outside the computational subspace. This applies architecture independent as all qubits are encoded within multilevel systems. Thus, leakage errors are most representative and typically occur at the same rates as computational errors, making their detection and correction an inevitable challenge. Our example quantum instrument recently played a central role in the experimental detection and correction of qubit loss embedded in a state-of-the-art QEC code [11]. There, the successful detection of a qubit loss event triggered a reconstruction routine, to restore the logical information on the remaining qubits. In the absence of loss, however, the reconstructed maps deviate from the aimed identity operation, owing to the in-sequence ancilla readout, resulting in nonunitary components. When forcing a unitary description, those mechanisms remain undetected

and likely diminish QEC performance. Hence, a proper quantum instrument reconstruction becomes essential.

Before we follow up with the characterization, we deliver essential insights into the nature of our loss detection unit. The dominant loss mechanism in a trapped-ion quantum processor is leakage from the qubit subspace $\{|0\rangle, |1\rangle\}$ to other electronic states, which can occur due to radiative decay from metastable electronic qubit states [65], in Raman transitions [66], or due to imperfections in spectroscopic decoupling pulses [67] when additional electronic states outside the computational subspace are used deliberately. Hence, loss can be induced in a controlled fashion by transferring part of the population from either computational basis state to an auxiliary level $D_{5/2}(m = +1/2) \equiv |2\rangle$, referred to as loss transition $R_{\text{loss}}(\phi)$, denoting a full coherent transfer in the case of $\phi = \pi$. We then apply the QND unit to map the information about a loss of the system qubit (q) onto an ancilla qubit (a), which is subsequently read out. In the language of quantum instruments, this means that one of two possible maps ("loss" or "no loss") has been applied to the system, with the classical index of the applied map stored in the qubit states $|0\rangle_a$ and $|1\rangle_a$ of the ancilla. Similar QND loss detection protocols have been devised using various other physical platforms [68–70].

Notably, for both ancilla outcomes, the system qubit is subject to a map that is CP, but in general not TP. This nonunitarity of the individual maps leads to several counterintuitive effects. For example, in the present case, the evolution of the system qubit differs from the identity map, even in the case where no loss is detected, if loss occurs asymmetrically, i.e., from only one of the computational basis states. More precisely, for loss restricted to occur from $|0\rangle$, the system qubit follows (up to normalization) a nonunitary evolution given by $\rho_q \mapsto \mathcal{E}_0 \rho_q \mathcal{E}_0^\dagger$ with

$$\mathcal{E}_0 = |1\rangle_q\langle 1| + \cos(\phi/2)\,|0\rangle_q\langle 0|\,, \tag{6}$$

considering the coherent loss operation $R_{\text{loss}}(\phi)$. This is a consequence of the information gain in the no-loss case, given by the ancilla measurement [11]. In either case, the reconstruction becomes challenging, since standard reconstruction techniques for quantum process tomography enforce the reconstructed processes to be completely positive and trace preserving, thereby suppressing the deviations from this condition characteristic for quantum instruments. This becomes evident in Fig. 3, where we compare the accuracy of quantum process reconstructions of the "no-loss" dynamics obtained via the standard MLE technique, referred to as the trace-constrained approach from Eq. (5) in contrast to the trace-unconstrained approach from Eq. (4). As a figure of merit we use the total variation distance between the measured frequencies and the measurement outcomes that are predicted from the reconstructed Choi operators. This highlights how the trace-constrained approach can fail to capture the dynamics; an error that might go unnoticed for maps that are close to trace preserving. Further notes on how common tomography fails to capture a quantum instrument's dynamics is subject to Fig. 14 of Appendix A 1.

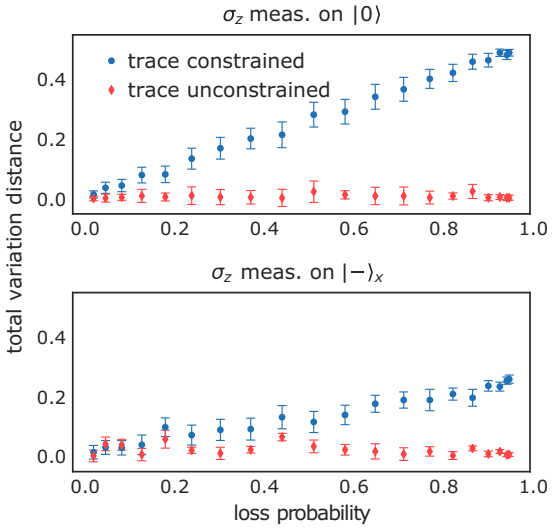

FIG. 3. Comparison of trace-constrained and trace-unconstrained tomography for the nonunitary map $\mathcal{E}_0$ from Fig. 2(b). We compute the total variation distance between directly measured frequencies and those predicted from the reconstructed Choi operators. Standard MLE from Eq. (5), referred to as the trace-constrained approach, increasingly fails to capture the underlying dynamics for higher loss probabilities, whereas the trace-unconstrained approach from Eq. (4) matches the predicted outcomes. Error bars correspond to one standard deviation of statistical uncertainty due to quantum projection noise. Further notes characterizing erroneous effects owing to a faulty quantum instrument reconstruction can be found in Fig. 14 of Appendix A 1.

V. EXPERIMENTAL RESULTS

We now discuss features associated in experiments with QND measurements that can only be captured using a full description as a quantum instrument. We start by characterizing our example instrument acting on a two-level system (qubit), followed by a complete characterization in a higher-dimensional Hilbert space that captures the entire dynamics of the QND measurement.

A. Implementation of the quantum instrument

We implement the circuit in Fig. 2(b) on a two-ion string studying several input states $\{|0\rangle_q, |-\rangle_{X,q} = (1/\sqrt{2})(|0\rangle_q - |1\rangle_q), |-\rangle_{Y,q} = (1/\sqrt{2})(|0\rangle_q - i\,|1\rangle_q), |1\rangle_q\}$ on the system qubit for a range of loss probabilities. We apply quantum state tomography for the runs that signal no-loss events, effectively applying the "no-loss" map $\mathcal{E}_0$ as given by Eq. (6). We focus on the no-loss outcome $\mathcal{E}_0$

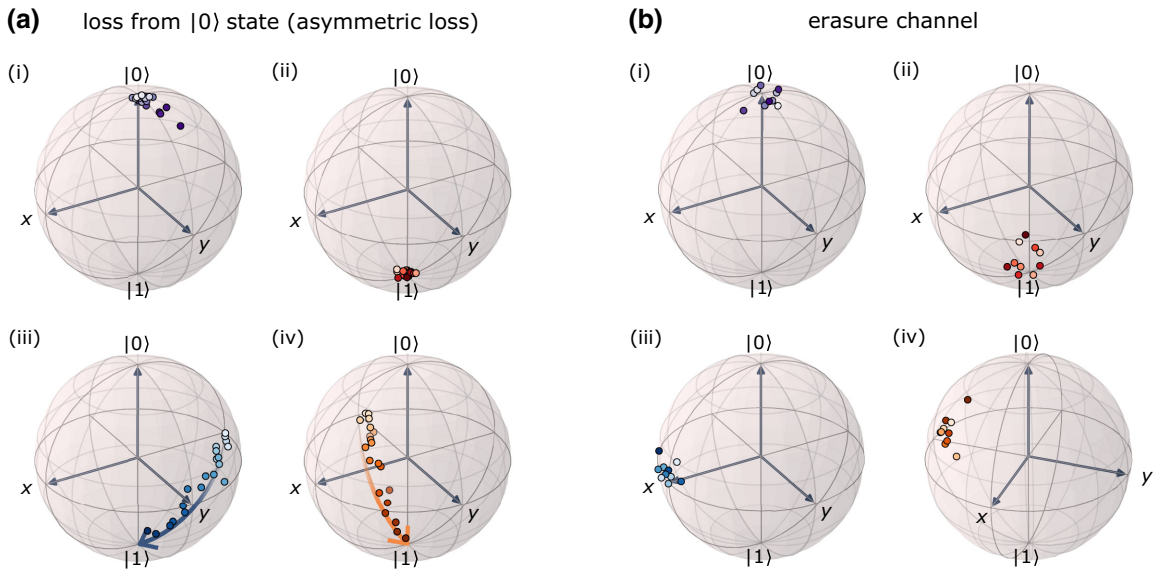

FIG. 4. Bloch vectors after undergoing QND detection in the no-loss case for different loss channels. (a) State vector evolution for asymmetric loss from $|0\rangle_q$ is captured by the color gradient, ranging from 0% loss (bright points) to 100% loss (dark points) for various input states (i) $|0\rangle_q$, (ii) $|1\rangle_q$, (iii) $|-\rangle_{X,q}$, and (iv) $|-\rangle_{Y,q}$. Notably, the Bloch vectors remain close to the surface of the sphere, independent of the loss probability; see the Appendix A 1. The initial superposition states $|-\rangle_{X,q}$ and $|-\rangle_{Y,q}$ are found transitioning to the basis state not affected by the loss. (b) The erasure channel is realized by consecutively inducing the same partial loss from $|0\rangle_q$ followed by $|1\rangle_q$ and postselecting to both no-loss cases, i.e., both ancilla's $|0\rangle_a$ outcome. Our results support the theory derivation of a map $\propto \rho$ leaving the initial states up to noise unaltered; see the Appendix A 1.

given that in a realistic scenario the system qubit would remain intact, as opposed to the loss case. We find that the superposition input states are *distorted* towards the basis state that is not affected by the loss with increasing loss probability; see Fig. 4(a). This is a consequence to the asymmetry of the loss, occurring only from one basis state, as detailed in Eq. (A9) in the Appendix A 1. Importantly, however, the states display no notable reduction in purity, regardless of the loss probability. More details are given in the Appendix A 1.

The archetypal description of a qubit loss channel features symmetric loss, often referred to as a *quantum erasure channel* [71], where loss occurs with a given probability, irrespective of the qubit state, and the position of the lost qubit is known. Experimentally, we realize this quantum erasure channel sequentially in two steps, by first inducing partial loss from $|0\rangle_q$ followed by its detection, and, conditional on detecting no loss in this first step, inducing the same amount of partial loss, but now from $|1\rangle_q$ in this second step. Experiments are conducted on a three-ion string using a single system qubit (q) and two ancilla qubits a_1 and a_2 as depicted in Fig. 2(c). By observing the evolution of the Bloch vectors in Fig. 4(b) we find that the initial state is preserved up to experimental noise, as derived in Eq. (A12) in the Appendix A 1. The purity is again found independent of the loss; see the Appendix A 1.

These findings are further corroborated by quantum process tomography characterizing the map describing the system qubit dynamics by using the unconstrained reconstruction approach of Eq. (4). In the case of the asymmetric loss previously discussed, the single-qubit Choi operators for the map $\mathcal{E}_0$ are close to the identity only given little loss on the order of a few percent and clearly deviate for higher loss, revealing their nonunitary behavior; see the left plot in Fig. 5(a) for a low-loss probability and the right plot for a high-loss probability. We note that a standard MLE approach would force unitary maps and thereby prevent the correct reconstruction not displaying this nonunitary behavior. In contrast, for the quantum erasure channel, for both the 2% and 61% loss cases, maps are found close to the identity following the theoretical predictions, depicted in Fig. 5(b).

For higher loss rates, however, we observe a deviation of the reconstructed Choi operator from the predicted channel, quantified by the fidelity between the reconstructed and ideal Choi operator shown in Fig. 5(c). For high loss rates, only few experimental cycles remain in the no-loss case. As a result, error terms, such as state-preparation-and-measurement (SPAM) errors, as well as errors in the implementation of the loss process contribute with a higher relative weight. We can model these additional error terms as depolarizing noise at the level of the Choi operator as a

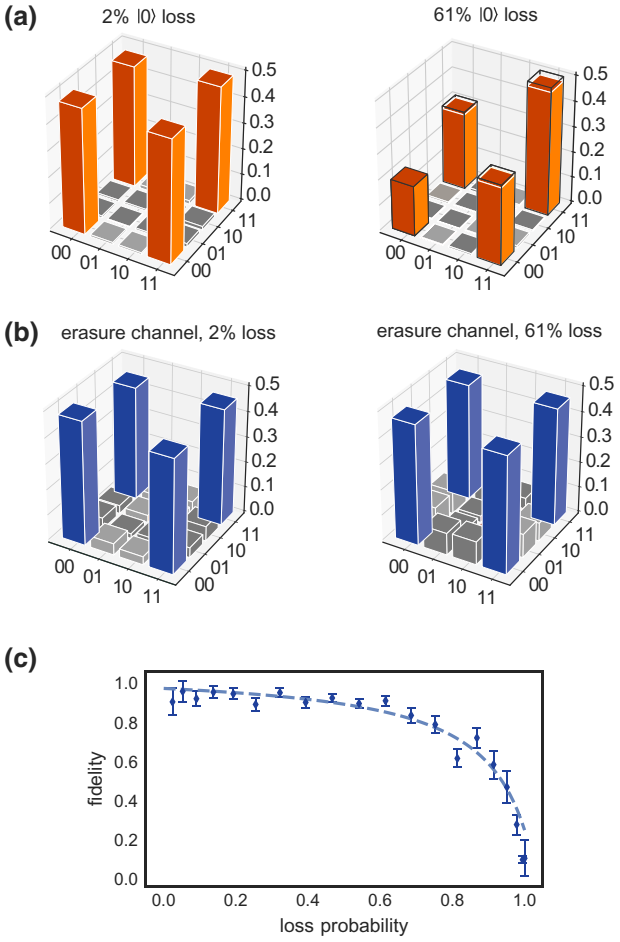

FIG. 5. Tomographic reconstruction of the maps characterizing our quantum instrument. (a) Single-qubit Choi operators in the elementary basis $\{|00\rangle_q, \ldots, |11\rangle_q\}$ describing the QND detection under loss from $|0\rangle_q$. Process fidelities compared to the ideal map for 2% and 61% losses read 0.97(1) and 0.98(1), respectively. Black boxes denote the ideal operator in the higher loss case. (b) On the erasure channel we receive the expected identity map for loss from both qubit states up to about 60% before errors start to dominate. (c) Corresponding process fidelities compared with ideal maps together with the decay model (dashed line) from Eq. (7).

function of the loss rate p_{loss}:

$$\begin{aligned}\Lambda_M(p_{\text{loss}}) \propto\ & (1-p_{\text{loss}})\cdot(1-p_e)\cdot(1-p_{\text{spam}})\cdot\Lambda \\ & + p_{\text{loss}}\cdot p_e\cdot(1-p_{\text{spam}})\cdot\mathbb{1}/4 \\ & + p_{\text{spam}}\cdot\mathbb{1}/4. \end{aligned} \tag{7}$$

Here Λ denotes the ideal Choi operator of the no-loss channel, $\mathbb{1}$ is the identity matrix, representing a fully depolarizing channel, p_e is a generic error rate of the erasure channel, and p_{spam} is the error rate due to SPAM errors. The first term of Eq. (7) describes the ideal channel where no loss happened and the QND detection worked, while the second term is a case where a loss happened, but

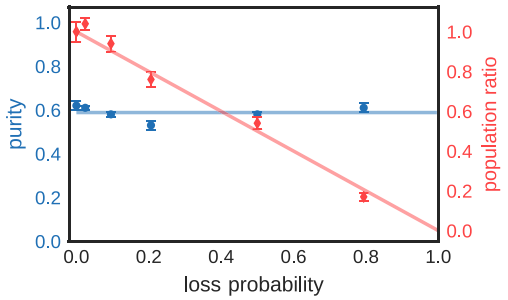

FIG. 6. Multiqubit entangled state undergoing QND detection in the no-loss case. As an input, we choose the four-qubit GHZ state $(1/\sqrt{2})(|0000\rangle_q + |1111\rangle_q)$. Loss is induced from $|0\rangle_{q,1}$ on system qubit 1. Results for purity (◯) and population ratio between the GHZ basis states $|0000\rangle$ and $|1111\rangle$ (◇) in analogy to the Bloch-vector picture (Fig. 4) are shown. The purity is found constant, while the population ratio increases towards higher loss probabilities, finally causing a *distortion* to state $|1111\rangle_q$ not affected by the loss. Errors correspond to one standard deviation of statistical uncertainty due to quantum projection noise.

the QND unit failed to detect it as such. The final term describes the contribution from SPAM errors. From a fit to the data, we find that $p_e = 0.09$ and $p_{\text{spam}} = 0.03$ captures the observed drop in fidelity well. From Fig. 5(c) we see that these effects become predominant for high loss rates, while for up to about 60%, a faithful reconstruction of the experimental Choi operator is possible.

The results presented so far cover a single system qubit and reveal potential obstacles of our quantum instrument tomography, which are generally transferable to other experiments utilizing QND measurements. We now go one step further by analyzing these effects on a multiqubit entangled state. Experiments are conducted using four system qubits, initialized in the Greenberger-Horne-Zeilinger (GHZ) state $(1/\sqrt{2})(|0000\rangle_q + |1111\rangle_q)$, accompanied by one ancilla. After state preparation, partial asymmetric loss from $|0\rangle_{q,1}$ on system qubit 1 is induced followed by its detection using the QND-detection unit. The "no-loss" evolution $\mathcal{E}_0$ is analyzed by four-qubit quantum state tomography. In Fig. 6 the states again show no significant reduction in purity (circles) over the range of measured loss probabilities and by that obscuring the nonunitary effect from our instrument. However, an asymmetric effect is displayed by computing the population ratio of the GHZ basis states $|0000\rangle_q$ and $|1111\rangle_q$ in Fig. 6 (diamonds) showing a *distortion* towards the basis state not affected by loss in analogy to the Bloch vectors in the single-qubit case. The underlying theory curve follows $1 - p_{\text{loss}}$, as can be seen from Eq. (6). The fidelity with the initial GHZ state further remains above 50% within one standard deviation of statistical uncertainty, thus certifying multipartite entanglement independent of the loss probability.

B. Qutrit dynamics and identification of failure modes

The full dynamics of our coherent loss process can be reconstructed by explicitly taking the loss level $|2\rangle_q$ into account. The state of the system ion needs then to be represented by a qutrit with basis states $\{|0\rangle_q, |1\rangle_q, |2\rangle_q\}$. We perform quantum process tomography on the combined system of data qutrit and ancilla qubit. This allows us to study both loss cases by distinguishing the maps dependent upon the ancilla state, and provides more fine-grained information on the microscopic error processes. The reconstructed Choi operators for both ancilla outcomes and various loss probabilities are given in Fig. 7(a). For the sake of clarity, the operators are color coded by peaks occurring in the absence of loss (blue), peaks denoting the partial loss rotation (orange), and erroneous peaks (red). The latter are restricted to the diagonal for simplicity. Note that these experimentally derived maps on the qutrit level are now faithful descriptions of the instrument, obtained

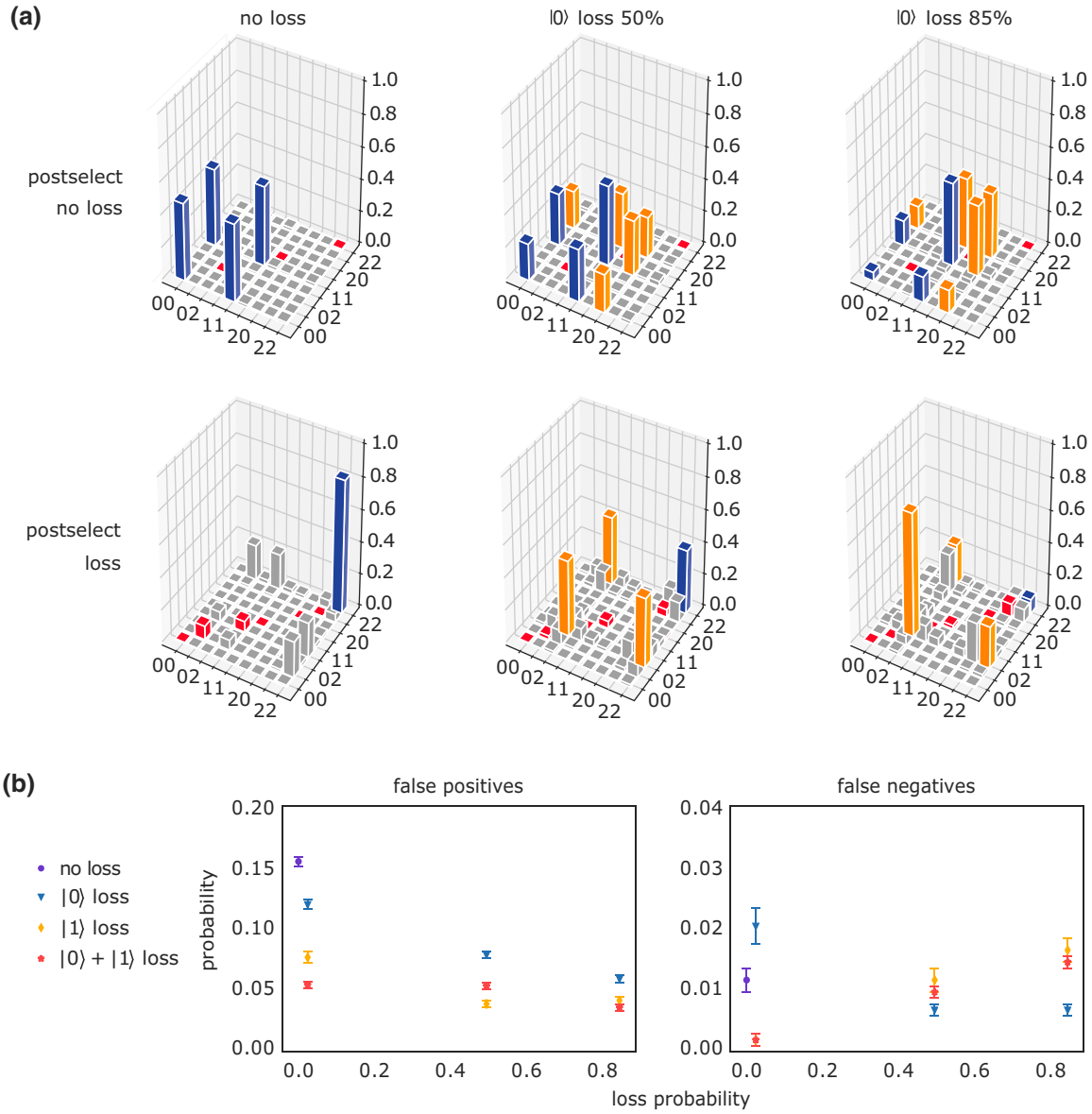

FIG. 7. Full-system dynamics from combined qutrit-ancilla quantum instrument tomography. (a) Choi operator of the system qutrit evolution in the elementary basis $\{|00\rangle_q, \ldots, |22\rangle_q\}$ after postselecting on the ancilla, revealing either loss case (rows) examined for different loss probabilities from $|0\rangle_q$ (columns). The tricolor Choi operators show peaks in the absence of loss (blue), peaks occurring due to partial loss (orange), and erroneous peaks (red). The latter are only color coded on the diagonal for visualization purposes. Process fidelities with the ideal map from top left to bottom right read $\{0.97(1), 0.96(1), 0.95(1), 0.83(1), 0.86(1), 0.84(1)\}$. (b) False-positive and false-negative rates extracted from raw data for loss states $\{|0\rangle_q, |1\rangle_q, 1/\sqrt{2}(|0\rangle_q + |1\rangle_q)\}$ versus the loss probability.

from the qubit-qutrit process that is indeed unitary; see Eq. (A5) in the Appendix A 1.

One key piece of information gained from the full tomography is the dominant failure modes of the experimental realization of the QND-detection unit. In the no-loss case, false negatives are retrieved from diagonal elements $\{|02\rangle_q, |12\rangle_q, |22\rangle_q\}$ corresponding to undetected rotations to level $|2\rangle_q$ outside the computational subspace. Likewise false positives in the loss case are retrieved from the elements $\{|00\rangle_q, |01\rangle_q, |10\rangle_q, |11\rangle_q, |20\rangle_q, |21\rangle_q\}$ corresponding to qubit rotations mistakenly assigned as loss. Note that, for standard tomography restricted to qubit levels, such fine-grained analysis would be precluded for two main reasons. First, the true population in the loss state of the system qutrit cannot be estimated independently from the ancilla outcome in the qubit description. Thus, one cannot reliably assign false-positive and false-negative events by postselecting on the ancilla since some erroneous population adds up to the main peaks $\{|00\rangle_q, |11\rangle_q\}$, blurring the information about the error origin. Second, when tracing over the ancilla, loss state $|2\rangle_q$ would be incoherently added to state $|1\rangle_q$, creating an nonphysical bias under which tomography is likely to break; see the Appendix A 1. For a more quantitative analysis, the corresponding false-positive and false-negative rates are depicted in Fig. 7(b). To avoid errors from the quantum instrument reconstruction, these rates are extracted from the raw data for three different loss states: $\{|0\rangle_q, |1\rangle_q, 1/\sqrt{2}(|0\rangle_q + |1\rangle_q)\}$. Notably, there is a significantly higher false-positive rate owing to their sensitivity on the entangling operation, implementing a correlated two-qubit rotation. This operation shows a higher error rate compared to single-qubit operations [44] and only plays a role in the no-loss case: the reason is that, as under loss, the action of the entangling operation, when it only acts on the ancilla qubit alone, is on purpose trivial and no longer induces a correlated qubit-qutrit flip process. Therefore, the loss map is left with the local bit-flip operations, explaining why false negatives are dominated by single-qubit errors, resulting in smaller rates. For loss detection in a QEC setting, we expect this asymmetry to be quite beneficial, as a false-positive event would merely trigger an unnecessary loss correction, while a false-negative event leads to an undetected loss, which can be catastrophic, i.e., leading directly to uncorrectable logical errors, as will be discussed in the next section.

C. Experimentally informed noise model

We now build noise models to characterize the QND-detection unit, which can then be used to study implications on QEC. From the above phenomenological discussion, we assume that the dominant contributions will come from false-positive and false-negative events, where the latter in particular can have a severe impact. However, extracting the respective rates from tomography data as in Fig. 7(b) in the presence of SPAM errors can be unreliable if these contributions are of the same magnitude. A rough estimate of the SPAM errors from tomography of the identity yields a fidelity of 0.96(2), which indicates that this is indeed the parameter regime we are dealing with here.

Hence, to describe imperfections in the QND loss detection unit, we instead focus on a microscopic noise model $\mathcal{E}_{\text{noise}}$ defined as (see the Appendix A 2)

$$\rho \mapsto \mathcal{E}_{\text{noise}}(\rho) = U_{\text{noise}} \rho U_{\text{noise}}^{\dagger}, \tag{8}$$

where the unitary $U_{\text{noise}} = R^{\text{MS}}(\alpha) R^{X}(\beta)$ describes the dominating error source as correlated bit flips with a rate of $p_{\text{corr}} = \sin^2(\alpha/2)$, resulting from systematic miscalibrations in the two-ion R^{MS} gate, and single-qubit flips with a rate of $p_{\text{single}} = \sin^2(\beta/2)$ from errors in the collective local rotations. Fitting channel $\mathcal{E}_{\text{noise}}$ to the experimental data returns values of $p_{\text{corr.}} = 0.045$ and $p_{\text{single}} = 2.47 \times 10^{-4}$, respectively; see the Appendix A 2. The fidelity of the experimental data with respect to this model in the no-loss case is 0.94, compared to 0.91 for the noiseless theory prediction.

In order to validate this model against generic hardware-agnostic noise models typically considered in the quantum information literature, we further add depolarizing and dephasing noise channels [72]. As discussed in detail in the Appendix A 2, by fitting a model that includes all four error channels to the experimental data, we again find the correlated bit-flip error to be dominant. The contributions from depolarizing and dephasing noise are consistently of the order of 0.01 and adding these terms does not significantly improve the fit to the data. From this analysis, we conclude that the microscopic model is the most suitable description of our experimental noise and the resulting imperfections in the QND loss detection, and we thus use this model in the following analysis of the impact of a faulty QND loss detection unit on QEC.

VI. IMPLICATION ON QUANTUM ERROR CORRECTION

In the context of QEC and the pursuit for robust and eventually fault-tolerant quantum computers, qubit leakage and loss errors are known to be particularly harmful to the performance of QEC codes, if they go unnoticed [47–49]. Dedicated protocols to fight qubit loss have been devised, including the four-qubit quantum erasure code [71], which has been implemented in the form of post-selective state analysis protocols using photons [73,74]. Moreover, protocols to cope with qubit loss in elementary quantum codes such as the five-qubit code [75] as well as topological QEC codes including the surface code [76] and color codes [67,77,78] have been developed.

Here, our aims are as follows. (i) To estimate the parameter regimes in which active qubit loss error correction and

detection is expected to reach break even, i.e., to become beneficial for low-distance QEC codes as currently pursued in various efforts [2,11,67,69,79–82]. (ii) Whereas most theory studies exclusively focus on the simple (and ideal) quantum erasure channel to describe loss, we are interested in illustrating the effect of various qualitatively different imperfections in the loss detection process on QEC performance, highlighting the importance of microscopically informed noise models of the components used in QEC of qubit loss. (iii) Finally, to predict the performance of QEC protocols by numerical simulations, it is desirable to develop *effective* few-parameter noise models, informed by experimental data, which can be simulated efficiently, e.g., using stabilizer simulations, to predict the performance of large-scale QEC codes built from noisy components. Here, we are particularly interested to which extent our faulty QND loss detection can be reliably substituted by efficiently simulatable noise models. Whereas the phenomenological studies from Fig. 7(b) pointed to false-positive and false-negative events as the dominant noise contributions, accurately extracting the respective error rates from tomography data is prohibited by SPAM errors. Instead, we here utilize the microscopic noise model covered by Sec. V C, incorporating the dominant error sources of correlated and single-qubit errors. This model best fits our noisy QND loss detection unit, especially in contrast to the widely used generic hardware-agnostic models of dephasing or depolarizing noise that lead to no notable contribution.

A. Qubit loss correction with color codes

To be concrete, we focus on the smallest two-dimensional color code [77], a seven-qubit stabilizer code equivalent to the Steane code [77,83], which is at the focus of current experimental efforts to achieve the break-even point of beneficial and fault-tolerant QEC with low-distance QEC codes [84–87]. The code is obtained by projecting the Hilbert space of seven qubits (Fig. 8) into the $+1$ eigenspace of six commuting stabilizer generators S_i^x and S_i^z $(i = 1, 2, 3)$ [see Fig. 8(a)] that define a two-dimensional code space hosting one logical qubit. Logical X and Z operators are defined as $X_L = \prod_{i=1}^{7} X_i$ and $Z_L = \prod_{i=1}^{7} Z_i$ and the logical basis states are $|0_L\rangle \propto \prod_{i=1}^{3}(\mathbb{1} + S_i^x)\,|0\rangle^{\otimes 7}$ and $|1_L\rangle = X_L\,|0_L\rangle$ (see the Appendix A 3). The code is a distance $d = 3$ QEC code ($d = 2n + 1$ with n the number of correctable computational errors), so that one arbitrary computational error (bit and/or phase flip error) on any of the physical qubits is correctable. Note that, besides computational errors, this code also allows one to correct the loss of any two of the seven physical qubits, or even the loss of some, though not all subsets of three or even four qubits (see the Appendix A 3 for more details). We note that, for each of the seven qubits forming the code, we incorporate state $|2\rangle_q$, i.e., adopt a qutrit description, and use this additional level to induce loss of a controllable amount via the coherent rotation in the subspace $\{|0\rangle_q, |2\rangle_q\}$ of the quantum instrument depicted in Fig. 2(b).

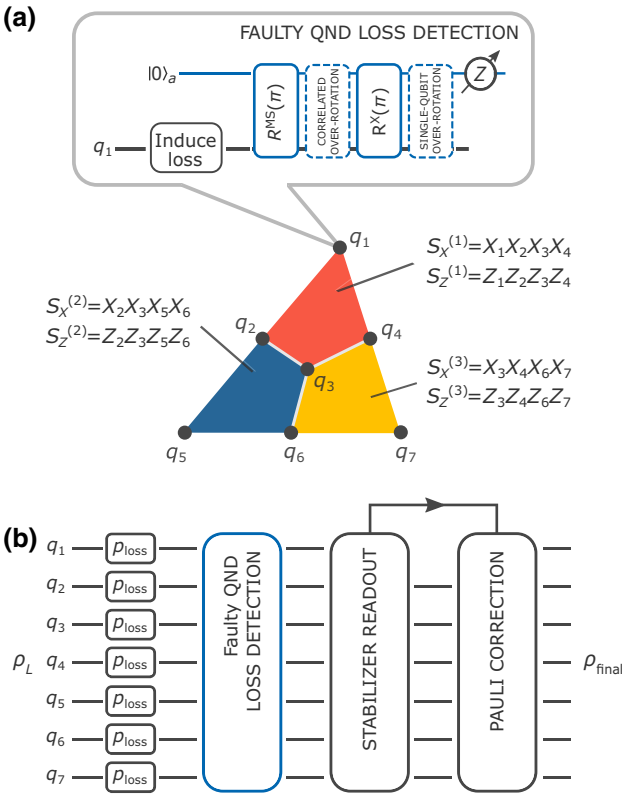

FIG. 8. Simulations on the faulty QND loss detection embedded in the seven-qubit color code. (a) A single logical qubit encoded on a triangular planar color code lattice formed of three interconnected plaquettes (lower part). The code space is formed by six stabilizer operators $S_x^{(i)}$ and $S_z^{(i)}$, each acting on a plaquette of four physical qubits [67]. Loss is subsequently detected on all code qubits using a faulty QND circuit (top part). We model this taking into account both correlated and single-qubit over-rotations, representing our leading error mechanisms by treating every qubit as a qutrit. (b) Single QEC cycle of qubit loss detection and correction, including initial controlled induction of loss, followed by faulty QND loss detection operations on the qubit subspace of all physical qutrits and stabilizer measurements triggering respective conditional Pauli corrections.

We then model one round of qubit loss error detection and correction, depicted in Fig. 8, as follows. Starting from an ideal (noise-free) logical state ρ_L of the seven-qubit code, qubit loss is induced with an independent and equal probability p_{loss} on each of the physical qubits of the register. Subsequently, a noisy QND loss detection unit is sequentially applied to each of the seven qubits, in order to detect the possible occurrence of loss. This faulty unit [Fig. 8(a)] is described by the microscopic noise model $\mathcal{E}_{\text{noise}}(\rho)$ in Eq. (8), where the main error sources are given

by correlated and single-qubit over-rotations with error rate p_{corr} and p_{single}, respectively.

Each data qubit, for which the QND measurement indicates the occurrence of a loss, is replaced by a fresh qubit in the computational basis state $|0\rangle_q$. This is followed by one round of possibly faulty measurements of all six stabilizers of the code. For simplicity, since our focus lies on the QND loss detection, here we model imperfections in each stabilizer measurement by a phenomenological noise model, in which the stabilizer measurement outcome is assumed to be faulty with probability q [88,89]. Since the four-qubit stabilizer operators are typically measured with a circuit involving (at least) four two-qubit gates, we work with 4 times the two-qubit error rate as the error rate of the stabilizer measurement, which results in $q = p_{\text{corr}}$, in what follows. Based on the obtained syndrome (± 1 stabilizer eigenvalues) from the measurement of the stabilizers, Pauli corrections are applied if needed (such a Pauli frame update can be done on the software level and is thus modeled as error-free). Finally, to determine the logical error rate, it is checked whether the original logical state ρ_L has been recovered or not, by evaluating the expectation value of the logical operator corresponding to the initially prepared encoded state.

B. Numerical results

Figure 9 shows the predicted logical error rate of the loss QEC cycle applied to all physical qubits as a function of the physical qubit loss rate p_{loss} for various error rates of faulty stabilizer measurements. At the current two-qubit gate infidelities and associated error rates $p_{\text{corr}} = 0.045$ and $p_{\text{single}} = 2.47 \times 10^{-4}$, the regime of beneficial loss correction, when the logical error rate falls below the physical loss rate p_{loss}, is not reachable. However, a moderate reduction of the two-qubit gate error rate by about 50%, from $p_{\text{corr}} = 0.045$ to about $p_{\text{corr}} = 0.023$, suffices to enter the regime where applying a cycle of faulty loss QEC outperforms storing information in a single physical qubit that can suffer loss.

Furthermore, Figs. 10(a) and 10(b) show the calculations of the logical error rate for the no-loss case $p_{\text{loss}} = 0$, which highlights the effects resulting from imperfections in the QND loss detection unit itself in a full QEC cycle. Here, the imperfections in the QND unit are implemented either with the coherent noise channel or an effective incoherent few-parameter Clifford noise model (details on the error models are given in the Appendix A 2). In Fig. 10(a) the logical error rate is shown as a function of the single-qubit over-rotation rate p_{single} for $p_{\text{corr}} = 0$ and it goes to zero as p_{single}^2 (black lines), as expected, representing the rate of weight-two bit-flip errors, which are uncorrectable by the distance-3 color code. In Fig. 10(b) instead the logical error rate is shown as a function of the correlated over-rotation rate p_{corr} for $p_{\text{single}} = 0$. In this case

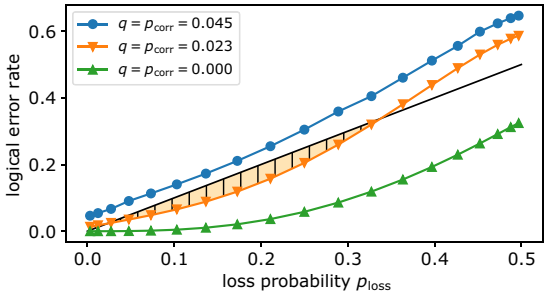

FIG. 9. Logical error rates simulated for a loss correction cycle of the seven-qubit color code with faulty stabilizer measurements. The logical error rates are shown as a function of the loss probability p_{loss} induced by the QND-detection scheme of Fig. 8 for different error rates q in the stabilizer readout. The black line (with equation $1 - p_{\text{loss}}$) represents the error rate when no encoding is performed. The logical error rates for the ideal case with no over-rotation errors in the QND loss detection unit are shown with green up-pointing triangles. Blue circles show the logical error rates when the QND-detection unit is simulated with over-rotation parameters ($p_{\text{corr}} = 0.045$, resulting in a stabilizer measurement error rate $q = 0.045$ and $p_{\text{single}} = 2.47 \times 10^{-4}$) coming from the experimental data. Data simulated with $q = p_{\text{corr}} = 0.023$ corresponding to an improvement in the R^{MS}-gate fidelity is shown with orange down-pointing triangles. In the region with $0.03 \lesssim p_{\text{loss}} \lesssim 0.33$, error correction is beneficial in protecting the logical states with respect to storing information in an unencoded single physical qubit.

the error rate goes to zero as p_{corr}^3 (black line), representing the rate of three bit-flip errors. The bit-flip errors from the correlated over-rotations result in false-positive events, where a nonlost qubit is substituted by a fresh qubit before the stabilizer measurement. Since two (detected) losses on any two qubits are correctable, some (detected) three-loss events are not; this results in the observed p_{corr}^3 scaling of the logical error rate. This highlights and explains the different sensitivities of the logical error rate to false-positive and false-negative events where the presence of false-negative events, i.e., overlooked losses, occurs for $p_{\text{single}} \neq 0$ and constitutes the more severe source of errors.

Finally, Figs. 10(c) and 10(d) show comparisons of the logical error rate for the two scenarios, where faults in the QND loss detection unit are modeled as coherent versus incoherent errors, respectively. When $p_{\text{corr}} \neq 0$ or $p_{\text{single}} \neq 0$, the logical error rate goes to a finite value when the loss probability $p_{\text{loss}} \to 0$ as error processes involving data qubit bit flips arise and lead to a finite failure rate of the error-correction cycle. Moreover, we observe that the incoherent approximation of the coherent error channel slightly underestimates the logical error rate, by a maximum relative factor of 0.51. This behavior is not unexpected, and has also been observed in other contexts, e.g., for an incoherent approximation of coherent crosstalk errors [90]. Overall, the results therefore indicate the reliability of the incoherent approximation of the faulty QND

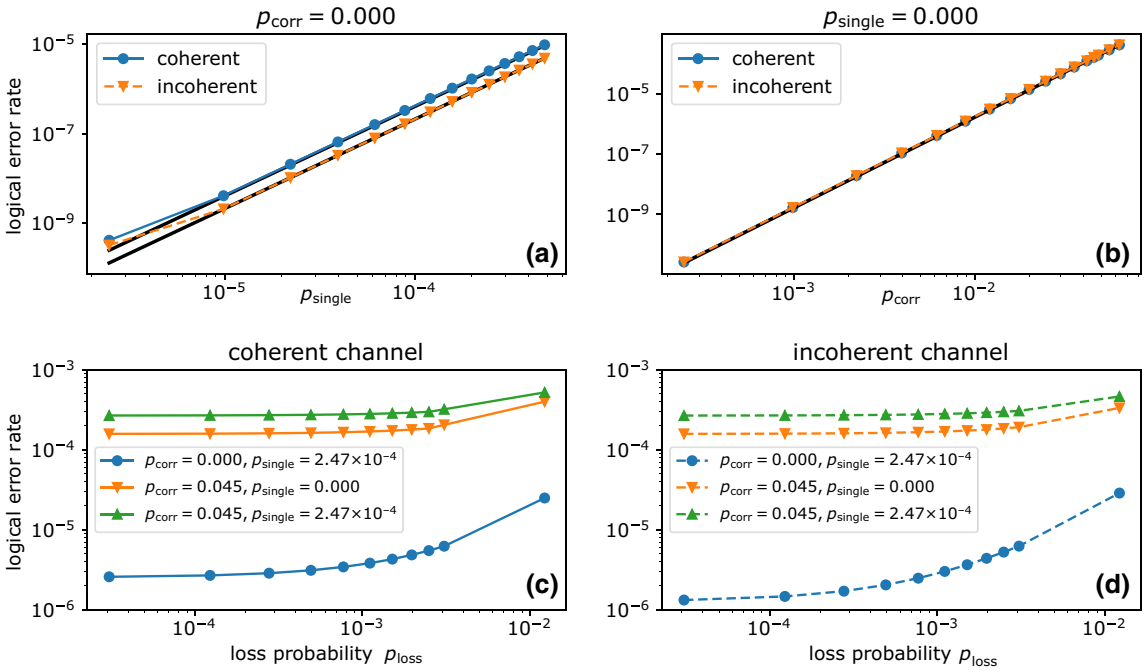

FIG. 10. Comparison between the coherent and incoherent implementations of the faulty QND loss detection unit. (a),(b). Logical error rates for $p_{loss} = 0$ as a function of (a) the single-qubit over-rotation rate p_{single} for $p_{corr} = 0$ and (b) the correlated over-rotation rate p_{corr} for $p_{single} = 0$ after a round of error correction of the seven-qubit color code following the scheme in Fig. 8 where the imperfections in the QND loss detection unit are implemented either with a coherent or an incoherent noise channel. (c) Logical error rate as a function of the loss probability when the faulty QND loss detection unit is modeled as a coherent channel. Panel (d) is the same as (c), but when errors in the QND loss detection are modeled as an incoherent Clifford channel.

loss detection unit in the QEC cycle. This is important as the latter incoherent model is efficiently simulatable and allows the study of faulty loss correction using stabilizer simulations of larger QEC codes.

VII. DISCUSSION AND OUTLOOK

Intermediate measurements with classical feedforward and the use of higher-dimensional quantum systems are rapidly becoming staple techniques in the toolbox of quantum information science. Beyond the obvious example of quantum error correction, the use of classical feedback to stabilize quantum systems [14,91] is an inevitable requirement for many high-precision applications. In the field of quantum computing the whole idea of measurement-based quantum computing is deeply rooted in measurements and feedforward, while quantum metrology often relies on weak or partial measurements, which must be described by quantum instruments. Similarly, in the field of quantum simulation, in-sequence measurements might be a way to use valuable quantum resources more efficiently in a hybrid quantum classical optimization setting [92,93]. What is common to all these tasks is that the measurement is nondestructive and imparts a backaction onto the postmeasurement state, which will depend on the outcome.

Faithfully characterizing the dynamics of such advanced operations will be key for the next generation of quantum devices, yet conventional methods fall short of this goal. The tools we develop here on the example of a QND measurement for qubit loss detection directly generalize to any quantum instrument, including the examples above. We find that the instrument picture captures essential features of the quantum dynamics, which in our case enable a detailed study of the effect of these instruments on quantum error correction. These results will inform progress on the correction of qubit losses and leakage errors, which represent a dominant obstacle on the path to quantum error correction above break even [51,94]. It will thus be interesting to apply these methods not only to fields where the measurement backaction has such a subtle influence, but also to fields where it is a key part of the operation, such as quantum metrology and sensing.

The presented techniques rely on tomographic reconstruction to guide the development of effective models for the studied quantum instruments. An interesting problem for future research would thus be to generalize and validate SPAM-free characterization techniques such as randomized benchmarking and gate set tomography [17] with respect to quantum instruments with low error rates.

DATA AVAILABILITY

The data underlying the findings of this work is available at [95].

ACKNOWLEDGMENTS

We gratefully acknowledge funding by the U.S. ARO Grant No. W911NF-21-1-0007. We also acknowledge funding by the Austrian Science Fund (FWF), through the SFB BeyondC (FWF Project No. F7109), by the Austrian Research Promotion Agency (FFG) Contract No. 872766, by the EU H2020-FETFLAG-2018-03 under Grant Agreement No. 820495, and by the Office of the Director of National Intelligence (ODNI), Intelligence Advanced Research Projects Activity (IARPA), via the U.S. ARO Grant No. W911NF-16-1-0070. This project has received funding from the European Union's Horizon 2020 research and innovation programme under the Marie Skłodowska-Curie Grant Agreement No. 840450, as well as by the European Research Council (ERC) via ERC Starting Grant QNets Grant No. 804247. It reflects only the authors' views, the EU Agency is not responsible for any use that may be made of the information it contains. We acknowledge the use of computational resources from the parallel computing cluster of the Open Physics Hub at the Physics and Astronomy Department in Bologna. T.M. and R.B. acknowledge support by the IQI GmbH.

D.V. and M.M. derived the theory results. R.S., A.E., L.P., M. Meth, M.R., P.S., and T.M. performed the experiments. R.S. analyzed the data. P.S., T.M., M.M., and R.B. supervised the project. All authors contributed to writing the manuscript.

APPENDIX: CHARACTERIZING QUANTUM INSTRUMENTS: FROM NONDEMOLITION MEASUREMENTS TO QUANTUM ERROR CORRECTION

The additional information presented here aims at providing further experimental and theoretical results supporting our findings in more detail. We start off by thoroughly deriving all maps underlying our QND loss detection unit in both cases of asymmetric loss and the quantum erasure channel. This will be complemented by further experimental data, all presented in Appendix A 1. We continue in Appendix A 2 by developing a noise model giving a well-founded description to our experimental limitations. Thereafter, those noise models form the basic building blocks to numerical simulations studying the implications of the loss detection in respect of quantum error correcting codes. We conclude with Appendix A 3 by giving more detailed derivations covering the loss treatment in the seven-qubit color code.

1. Quantum instrument: QND loss detection

This section gives a more thorough introduction to QND detection, serving as our quantum instrument working example, by deriving all maps relevant to our studies. Then, additional experiments are presented addressing the demonstration of QND-detection's principal working ability complemented by results on the higher-dimensional process tomography fully characterizing its underlying maps.

As loss on our setup naturally occurs at rates similar to those of single-qubit errors, we introduce it in a controlled fashion. For instance, from the system qutrit's (q) state $|0\rangle_q$, loss can be induced by coherently transferring part of the population outside the computational subspace into $D_{5/2}(m=+1/2)=|2\rangle_q$ via the rotation

$$R_{\text{loss}}(\phi) = |1\rangle\langle 1|_q + \cos(\phi/2)(|0\rangle\langle 0|_q + |2\rangle\langle 2|_q) + \sin(\phi/2)(|0\rangle\langle 2|_q - |2\rangle\langle 0|_q). \tag{A1}$$

The loss rate ϕ relates to the loss probability via $p_{\text{loss}} = \sin^2(\phi/2)$. Note that loss in general can be induced through an arbitrary state $\alpha|0\rangle_q + \beta|1\rangle_q$ with $|\alpha|^2+|\beta|^2=1$ using a single coherent rotation on the system qutrit before and its inverse after the loss rotation $R_{\text{loss}}(\phi)$. To detect loss, two full entangling $R^{\text{MS}}(\phi/2)\cdot R^{\text{MS}}(\phi/2) = R^{\text{MS}}(\phi)$ couple to the ancilla and system qutrit and realize a collective bit flip only if both qubits are present in their computational subspace:

$$\begin{aligned} R^{\text{MS}}(\phi) &= \exp\left(-i\frac{\phi}{2}X_aX_q\right) \\ &= (\cos(\phi/2)(\mathbb{1}_a\otimes\mathbb{1}_q - |2\rangle\langle 2|_q) \\ &\quad - i\sin(\phi/2)X_aX_q) + |2\rangle\langle 2|_q \end{aligned} \tag{A2}$$

with

$$\mathbb{1}_a = \begin{pmatrix}1&0\\0&1\end{pmatrix},\quad \mathbb{1}_q = \begin{pmatrix}1&0&0\\0&1&0\\0&0&1\end{pmatrix},\quad X_a = \begin{pmatrix}0&1\\1&0\end{pmatrix},$$
$$X_q = \begin{pmatrix}0&1&0\\1&0&0\\0&0&0\end{pmatrix}. \tag{A3}$$

On the other hand, if the system qutrit occupies a state outside the computational subspace, for instance in $|2\rangle_q$, the R^{MS} gate is subject to an identity operation, which can be seen from the argument of its exponential $X_iX_i=\mathbb{I}$ acting merely on the ancilla qubit. This follows a collective bit flip

$$\begin{aligned} R_a^X(\pi) &= -i(|0\rangle\langle 1|_a + |1\rangle\langle 0|_a), \\ R_q^X(\pi) &= |2\rangle\langle 2|_q - i(|0\rangle\langle 1|_q + |1\rangle\langle 0|_q). \end{aligned} \tag{A4}$$

Consequently, in the absence of loss the effect of the R^{MS} gate is undone, whereas under loss, the ancilla qubit gets excited by the final bit flip, signaling the event of loss. The overall unitary combining loss operation and QND detection is given by

$$\begin{aligned} U &= R_a^X(\pi) R_q^X(\pi) R^{\mathrm{MS}}(\pi) R_{\mathrm{loss}}(\phi) \\ &= \mathbb{1}_a \otimes U^{(0)} + X_a \otimes U^{(1)} \end{aligned} \tag{A5}$$

with

$$\begin{aligned} U_q^{(0)} &= |1\rangle\langle 1|_q + \cos(\phi/2)\,|0\rangle\langle 0|_q + \sin(\phi/2)\,|0\rangle\langle 2|_q\,, \\ U_q^{(1)} &= \sin(\phi/2)\,|2\rangle\langle 0|_q - \cos(\phi/2)\,|2\rangle\langle 2|_q\,. \end{aligned} \tag{A6}$$

Taking the additional loss state $|2\rangle_q$ on the system qubit into account and, by that, extending the view from qubit to qutrit, one ends up with a unitary process fully describing this quantum instrument. We emphasize that on the qutrit level the entire dynamics of our detection unit can be captured, which is well exploited by the experiments from Fig. 7 in the main text

However, to pick up the discussion on the nonunitary effects potentially leading to unwanted and erroneous mechanisms, we restrict our view again to the qubit level and further assume that no population is initially present in $|2\rangle_q$. Hence, the operators $U_q^{(0)}$ and $U_q^{(1)}$ reduce to

$$\begin{aligned} A_q^{(0)} &= |1\rangle\langle 1|_q + \cos(\phi/2)\,|0\rangle\langle 0|_q\,, \\ A_q^{(1)} &= \sin(\phi/2)\,|2\rangle\langle 0|_q\,, \end{aligned} \tag{A7}$$

leading to single-qubit processes describing the QND detection restricted to the system qubit. We can describe both maps $\{A_q^{(0)}, A_q^{(1)}\}$ by two trace nonincreasing CP maps $\mathcal{E}_0$ and $\mathcal{E}_1$,

$$\begin{aligned} \mathcal{E}_0 &: \rho \mapsto A_q^{(0)} \rho A_q^{(0)\dagger}, \\ \mathcal{E}_1 &: \rho \mapsto A_q^{(1)} \rho_q A_q^{(1)\dagger}, \end{aligned} \tag{A8}$$

acting on the system qubits as

$$\rho \mapsto |0\rangle\langle 0|_a \otimes \mathcal{E}_0(\rho) + |1\rangle\langle 1|_a \otimes \mathcal{E}_1(\rho), \tag{A9}$$

where the two maps are together unitary again. It is noteworthy that the no-loss map $\mathcal{E}_0$ initially starting from the superposition state $1/\sqrt{2}(|0\rangle_q + |1\rangle_q)$ would be transitioning to $|1\rangle_q$ as the loss probability from $|0\rangle_q$ increases, which is subject to Fig. 4(a) in the main text. Only for very little loss, $\phi \sim 0$, the no-loss map converges to an identity operation.

Next to having loss asymmetrically with respect to either computational basis state $\{|0\rangle_q, |1\rangle_q\}$, we follow a different, often utilized, scenario called the quantum erasure channel [71]. Its circuit is depicted in Fig. 2(c) of the main text. First, partial loss is induced from $|0\rangle_q$ followed by its detection. The protocol only continues in the absence of loss by inducing the same partial loss from the other qubit state $|1\rangle_q$ together with its detection. The second part of the map can be expressed via $\{\tilde{A}_q^{(0)}, \tilde{A}_q^{(1)}\}$, where we swap the roles of $|0\rangle_q$ and $|1\rangle_q$. Thus, the quantum erasure channel can be described using the map

$$\begin{aligned} \rho \mapsto\ & (1-p_L)(1-\widetilde{p}_L)\widetilde{A}_q^{(0)} A_q^{(0)} \rho A_q^{(0)\dagger} \widetilde{A}_q^{(0)\dagger} \\ & + (1-p_L)\widetilde{p}_L \widetilde{A}_q^{(1)} \rho \widetilde{A}_q^{(1)\dagger} + p_L A_q^{(1)} \rho A_q^{(1)\dagger} \end{aligned} \tag{A10}$$

with probabilities p_L and $\widetilde{p}_L$ for any arbitrary input state $\alpha|0\rangle_q + \beta|1\rangle_q$ given by

$$p_L = |\alpha|^2 \sin^2(\phi/2), \qquad \widetilde{p}_L = \frac{|\beta|^2 \sin^2(\phi/2)}{|\alpha|^2 \cos^2(\phi/2) + |\beta|^2}. \tag{A11}$$

In this case the process reduces to

$$\rho \mapsto \cos^2(\phi/2)\rho + \sin^2(\phi/2)\,|2\rangle\langle 2|_q\,, \tag{A12}$$

where the effect of the loss is proportional to the arbitrary input state ρ, indicating that after normalization the initial state can be retrieved independently of the loss probability.

The basic idea of this quantum instrument is the detection of qubit loss, i.e., unwanted leakage to levels outside the computational subspace, that in a realistic scenario would be followed by its correction, representing the scope of our foregoing work [11]. To give the rather formal discussion a physical meaning, we demonstrate the unit's working principle. Partial loss induced from $|0\rangle_q$ via the loss transition $R_{\mathrm{loss}}(\phi)$ is continuously increased and subsequently detected. Note that both qubits are read out yielding their populations in the upper $|D\rangle$-state manifold referring to directly measured loss in the case of the system qubit and detected loss for the ancilla qubit. In Fig. 11 results are presented for individual and repeated loss detection employing up to two ancilla qubits. Slopes extracted from the linear fit in the repeated detection read 0.938(9) and 0.944(12) for ancillae a_1 and a_2, respectively. On the individual readouts we get 0.977(2) and 0.995(2) with a resonant crosstalk to the ancilla not participating of 0.005(1) and 0.003(1), respectively. When utilizing a_2, we end up with a higher detection efficiency because of a better performing $R_{i,j}^{\mathrm{MS}}$ gate on the particular ion pair. Two hundred cycles are taken on this measurement. Errors correspond to one standard deviation of statistical uncertainty due to quantum projection noise.

Next, we complement the results from Fig. 4(a) in the main part revealing a pull towards the state not affected from asymmetric loss by further demonstrating that the purity $\mathrm{Tr}(\rho^2)$ of the associated reconstructed states remains constant across the entire loss probability range;

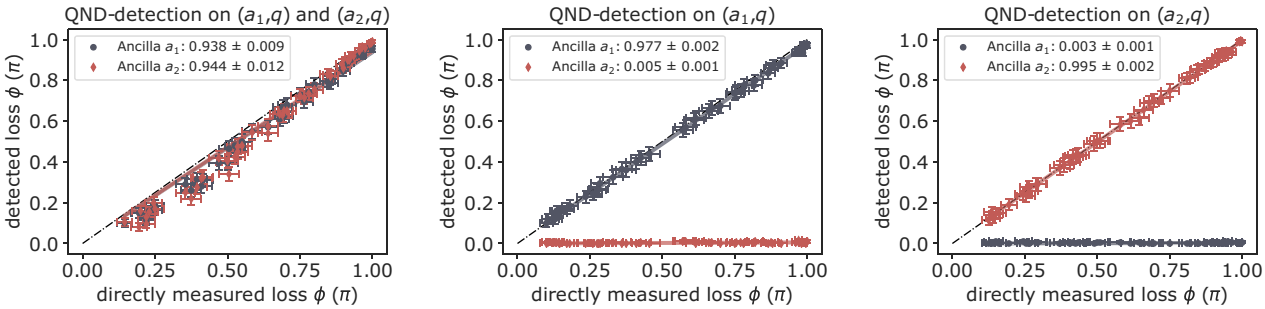

FIG. 11. Investigating the performance of the QND-detection unit according to Fig. 2(b) in the main text. Population in the $D_{5/2}$ state for the system qubit (directly measured loss) versus transferred excitation on the ancilla qubit (detected loss) in the case of detecting loss repeatedly using both ancilla qubits a_1 and a_2 (left), solely with ancilla a_1 (middle), and ancilla a_2 (right). The imprinted detection efficiencies demonstrate reliable loss mapping onto the ancilla qubit and its readout by means of QND. Errors correspond to one standard deviation of statistical uncertainty due to quantum projection noise.

see Fig. 12(a). The purity value is found independent of the loss and therefore underlining at first glance a correct experimental outcome, whereas only in the Bloch sphere picture [Fig. 4(a)] deviations due to the nonunitary map become visible. Likewise, considerations have been done on the erasure channel, previously discussed in Fig. 4(b) and similarly producing purity values independent of loss, as can be seen in Fig. 12(b).

Next, we estimate the detection correlation of a single loss event by two repeated detections. Such system capabilities emphasize the work on the erasure channel and, more generally, become relevant in a realistic scenario demanding several consecutive readouts, especially when embedded in QEC codes. In Fig. 13 positive correlation occurs for a certain shot when both ancilla qubits agree upon a certain loss event. Furthermore, the data on the repeated readout allow us to quantify false-positive and false-negative rates, manifesting important failure modes of our detection unit. Again, false-positive rates dominate owing to their strong sensitivity on the entangling R^{MS} gate, as was the case in Fig. 7(b) in the main text. One hundred cycles for $|0\rangle_q$ loss and 200 cycles for $1/\sqrt{2}(|0\rangle_q + |1\rangle_q)$ loss are taken on this measurement. Errors correspond to one standard deviation of statistical uncertainty due to quantum projection noise.

We switch our consideration from qubit to the qutrit level and resume the discussion on the process tomography covering both the ancilla qubit and system qutrit from Fig. 7(a) in the main text. Thereby all presented Choi operators are postselected upon the ancilla outcome denoting the qutrit maps separated by both loss cases. This has the advantage of unitary operators describing the full dynamics of the system qutrit in either loss case that moreover gives an estimation on the QND-detection's dominant failure mode, namely false-positive and false-negative rates. As discussed in detail in the main part of the paper, standard tomography restricted to the qubit level prevents us from getting such fine-grained analysis for two main

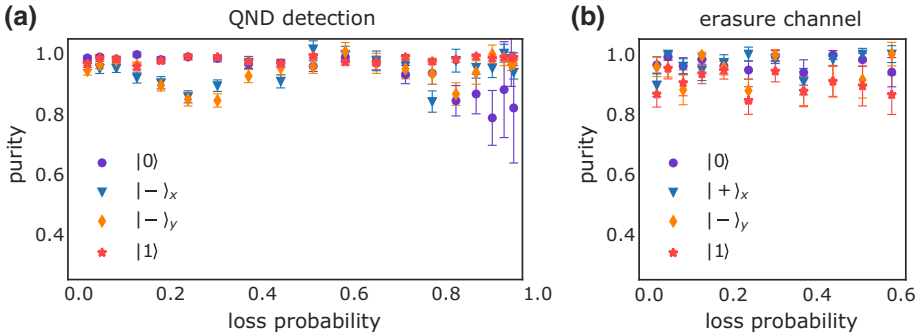

FIG. 12. Purity of a single system qubit after undergoing QND detection in the no-loss case for different loss channels. (a) After a single QND detection with loss from $|0\rangle_q$, we find purity values unaffected by the amount of loss for all of the given input states. At high loss probabilities, tomography becomes unreliable due to the low count rates. Furthermore, the superposition states show systematic drifts beyond the given statistical errors, which however do not affect the results. (b) The erasure channel is realized by consecutively inducing the same partial from $|0\rangle_q$ followed by $|1\rangle_q$ and postselecting to both ancilla $|0\rangle_a$ outcomes. The purity of the output state is again unaffected by loss for any of the probed input states. Errors correspond to one standard deviation of statistical uncertainty due to quantum projection noise.

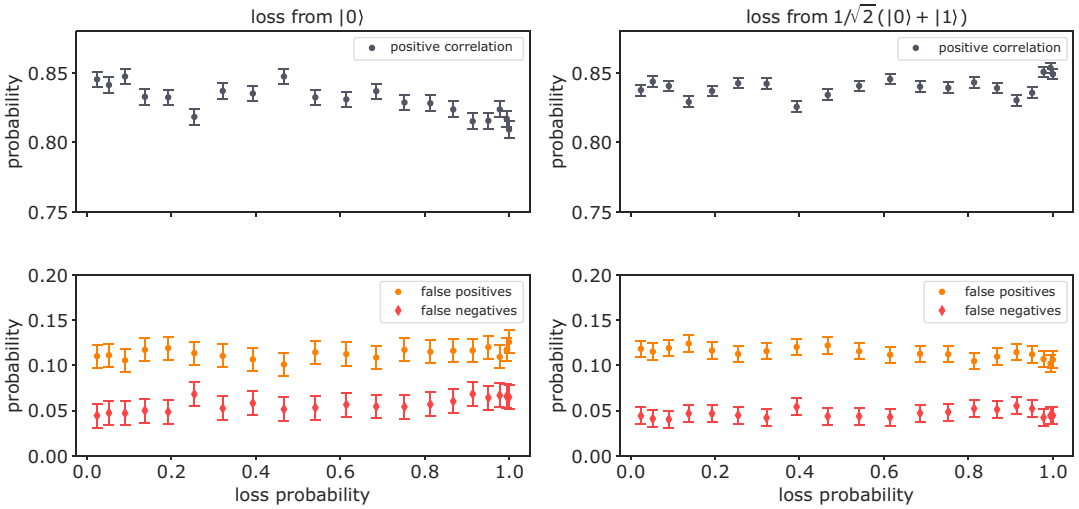

FIG. 13. Correlations between two repeated QND detections according to Fig. 2(b) in the main text. Loss on the system qubit is induced from the imprinted states followed by two repeated detections using ancillae a_1 and a_2. A positive correlation refers to successfully detecting the same loss event twice, whereas faulty assignments can be separated into false-positive and false-negative events; shown in the lower figure part. Errors correspond to one standard deviation of statistical uncertainty due to quantum projection noise.

reasons. First, reliably assigning false-positive and false-negative events is not possible when postselecting by the ancilla qubit's measurement outcome. Second, when tracing over the ancilla, the loss state $|2\rangle_q$ is incoherently added to the qubit state $|1\rangle_q$, creating an nonphysical bias under which tomography is likely to break, as demonstrated in Fig. 14. Here, we distinguish between tracing before and after tomography reconstruction. On the one hand, when directly tracing on the raw data and subsequently reconstructing the map, it includes coherences owing to the reconstruction technique forcing physical properties. On the other hand, when tracing after process reconstruction, coherences on $|01\rangle_q$ vanish. Both cases draw attention to potential risks on how commonly known process tomography fails to describe quantum instruments.

In the context of the numerical simulations covering implications on QEC however, we make use of the full map capturing the combined ancilla-qutrit dynamics together with the noise models; further discussed below. We present experimentally estimated ancilla-qutrit Choi operators for various loss probabilities in Fig. 15 using the elementary basis according to $\{|0000\rangle_{a,q}, \ldots, |1212\rangle_{a,q}\}$. The process tomography of every loss probability required $54 \times 12 = 648$ experimental settings. For the sake of clarity, we plot ideal Choi operators (left column) and the experimental ones (right column) for various loss probabilities separated by rows side by side. Color and saturation refer to the argument and absolute value of the complex matrix entries. Process fidelities with the ideal Choi operator from top to bottom read $\{0.91(1), 0.89(1), 0.85(1)\}$, referring to the loss probabilities $\{0\%, 50\%, 85\%\}$. One hundred cycles are taken for each experiment. In the no-loss case the expected controlled $\hat{X}_a$ operation signaling a loss event whenever the system qubit occupies level $|2\rangle_q$ is clearly reproduced, as expressed by Eq. (A5) derived at the beginning of this section.

Finally, we present additional data on the system qutrit process tomography according to Fig. 16(a) and loss induced from $|0\rangle_q$ and $|1\rangle_q$ presented in Figs. 17 and 18, respectively. We emphasize that here, similar to the qubit level, certain coherences vanish when tracing over the ancilla, which is no longer covered by the process tomography. Still, the dynamics on the system qutrit clearly captures the population transfer from either basis state $\{|0\rangle_q, |1\rangle_q\}$ to the loss level $|2\rangle_q$. Furthermore, a change in the asymmetric behavior between loss from $|0\rangle_q$ and $|1\rangle_q$ becomes distinctly visible in the qubit subspace.

For the sake of completeness, we present similar Choi operators on the repeated loss detection in Fig. 19, consecutively mapping the same loss event to two different ancilla qubits; shown for loss from $|0\rangle_q$. As the reconstructed Choi operators follow the expected behavior previously observed, their fidelities turn out slightly lower compared to Fig. 17, as expected due to the more complex experiment.

2. Noise model on QND loss detection

Here, we study various noise models in order to find the best suitable description of the experimental limitations underlying our QND detection. Although very small contributions will be precluded by SPAM errors, the resulting models give us a rough estimate as a guide for where to look at upon which a microscopic noise model

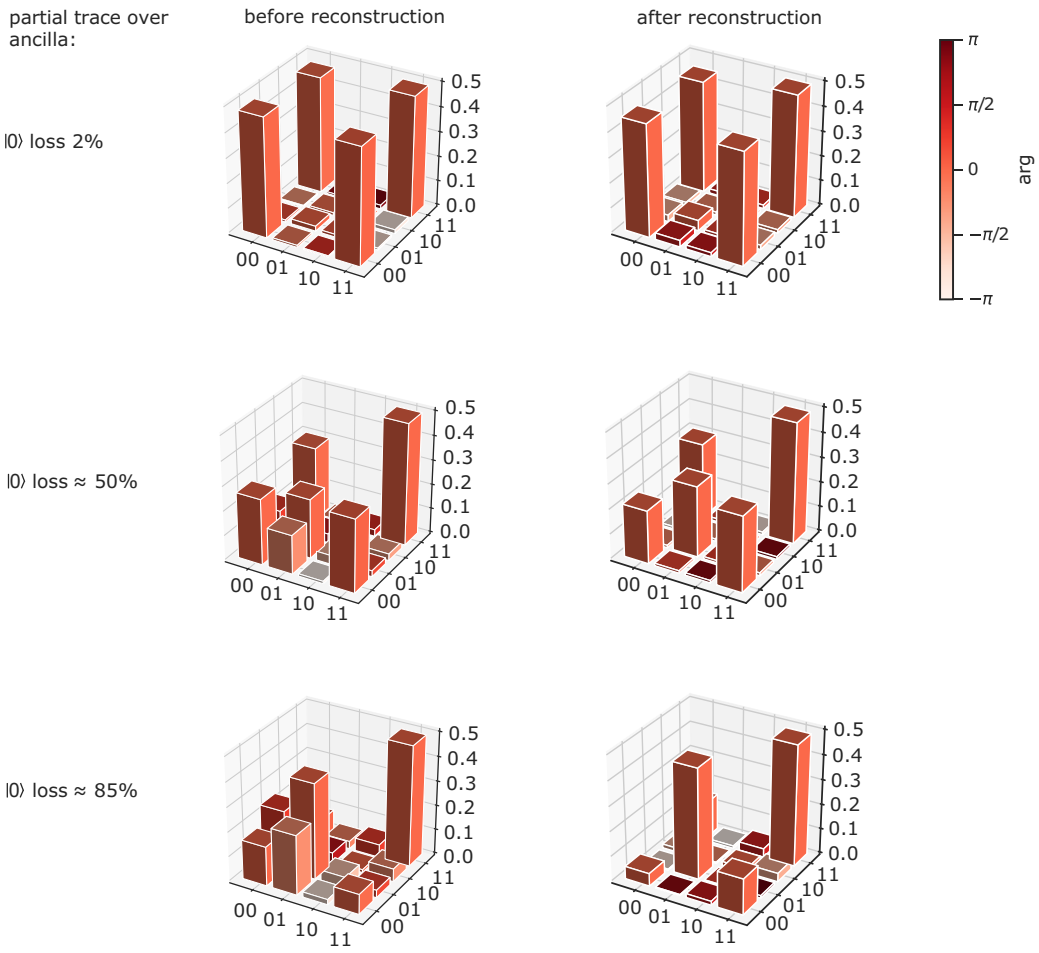

FIG. 14. Potential risks on system qubit process reconstruction when partial tracing the ancilla qubit. Left column: partial tracing before reconstructing the map directly on the raw data, previously used in Fig. 7 of the main part. In this case, the loss level $|2\rangle_q$ is incoherently added onto state $|1\rangle_q$. Coherences present in $|01\rangle_q$ originate from the reconstruction technique, forcing physical properties. Right column: postselecting from the already reconstructed qubit-qutrit maps presented in Fig. 15. In contrast to before coherences on $|01\rangle_q$ vanish, whereas the nonphysical bias remains.

for the numerical simulations can be developed. Getting more insights on these error mechanisms is essential when observing implications of the quantum instrument in the context of QEC protocols and is further an essential building block towards fault-tolerant quantum computation; see Sec. VI of the main text.

We refer to Eq. (A5) from above and express the action of the ideal QND map U under a given loss rate ϕ acting on the combined ancilla-qutrit system in terms of the Choi operator $\rho^{\mathrm{CJ}} = \mathbb{1} \otimes U \cdot |\Phi_+\rangle \langle\Phi_+| \cdot \mathbb{1} \otimes U^\dagger$, where $|\Phi_+\rangle \langle\Phi_+|$ is the maximally entangled state of two copies of the ancilla-qutrit system. An erroneous channel $\mathcal{E}_{\mathrm{noise}}$ transforms the Choi operator ρ^{CJ} to $\rho^{\mathrm{CJ}}_{\mathrm{noise}} = (\mathbb{1} \otimes \mathcal{E}_{\mathrm{noise}})(\rho^{\mathrm{CJ}})$. Noise rates entering $\mathcal{E}_{\mathrm{noise}}$ for given model parameters are then extracted by minimizing the distance between modeled noisy Choi operators $\rho^{\mathrm{CJ}}_{\mathrm{noise}}$ and the experimentally determined ones $\rho^{\mathrm{CJ}}_{\mathrm{exp}}$ from Fig. 15. As a measure for the distance in the cost function, we minimize the infidelity:

$$||1 - \mathcal{F}(\rho^{\mathrm{CJ}}_{\mathrm{exp}}, \rho^{\mathrm{CJ}}_{\mathrm{noise}})||. \tag{A13}$$

Our initial considerations covered the study of the QND-detection's failure modes, i.e., false-positive and false-negative rates both quantified in the main part of the paper. Measuring process tomography however comes with overhead in the form of preparation and measurement gates followed by two consecutive detections at the end of each experiment required for reading out the qutrit's state. Therefore, SPAM errors are not to be neglected and lead to a significant bias on false-positive and false-negative rates. With this in mind, we put the failure modes aside and focus on experimental limitations instead. In the following, we consider as models for $\mathcal{E}_{\mathrm{noise}}$ a depolarizing channel, a dephasing channel, and coherent two- and single-qubit over-rotations.

Depolarizing and dephasing channels.—We start off by testing the agnostic models, namely depolarizing and dephasing channels as those represent error mechanisms typically considered in the field of quantum computation [72]. The effect of the latter can be understood by losing phase information between the quantum states involved. Coherences get lost and an arbitrary single-qubit state in the Bloch sphere picture would finally shrink onto the Z axis as no phase information is left. Depolarizing noise can be considered as simultaneous dephasing in the X, Y, and Z bases, eventually leading to a complete mixed state that, for a single qubit, can be illustrated by shrinking

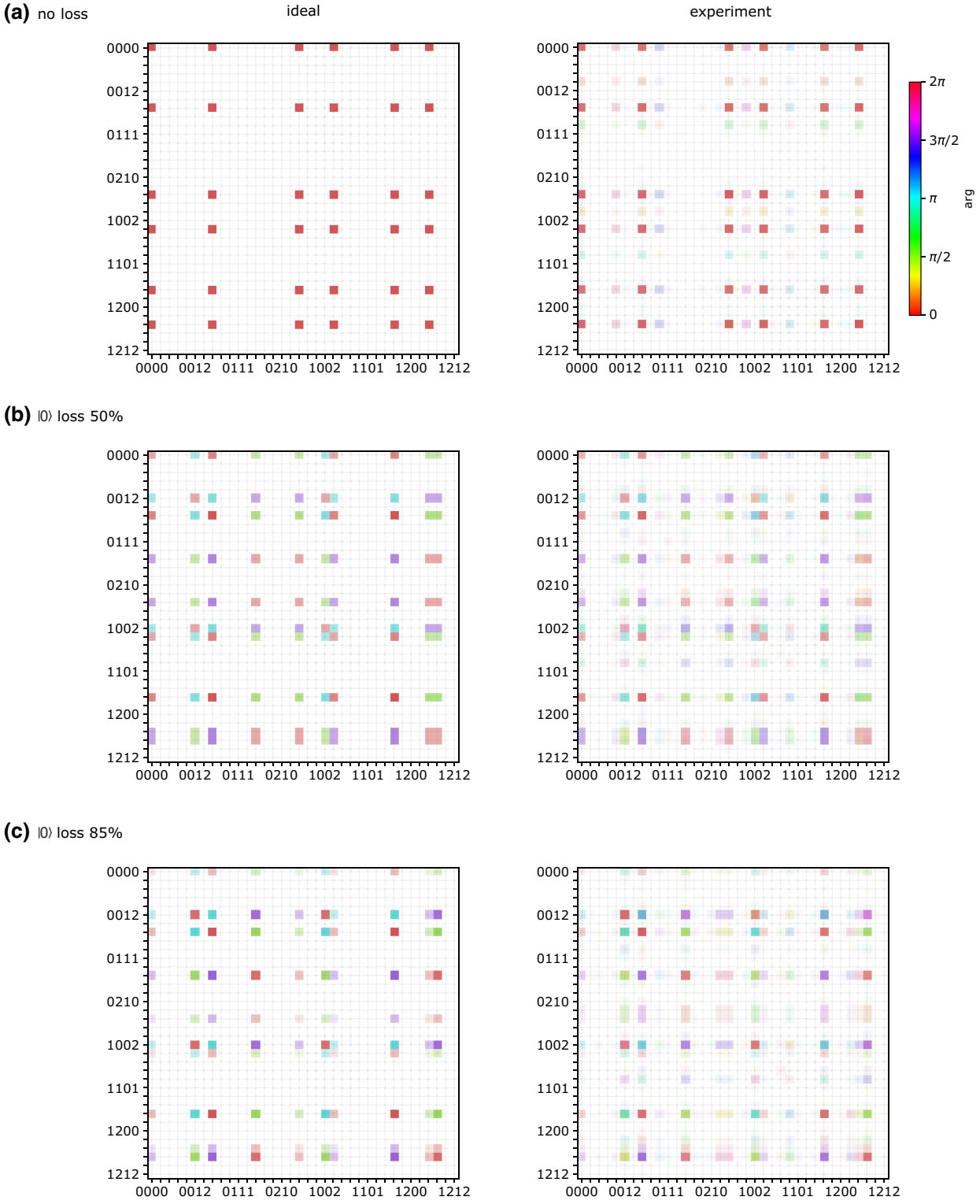

FIG. 15. Combined process reconstruction on the ancilla-qutrit system according to Fig. 16(b). The resulting Choi operators (right column) denoted in the elementary basis ($\{|0000\rangle_{a,q}, \ldots, |1212\rangle_{a,q}\}$) describe the whole dynamics of the QND-detection unit under loss from $|0\rangle_q$. Hue relates to phase according to the top right color bar and saturation to the absolute value of the complex entries. Process fidelities with the ideal Choi operators (left column) from top to bottom read $\{0.91(1), 0.89(1), 0.85(1)\}$. Errors correspond to one standard deviation of statistical uncertainty due to quantum projection noise.

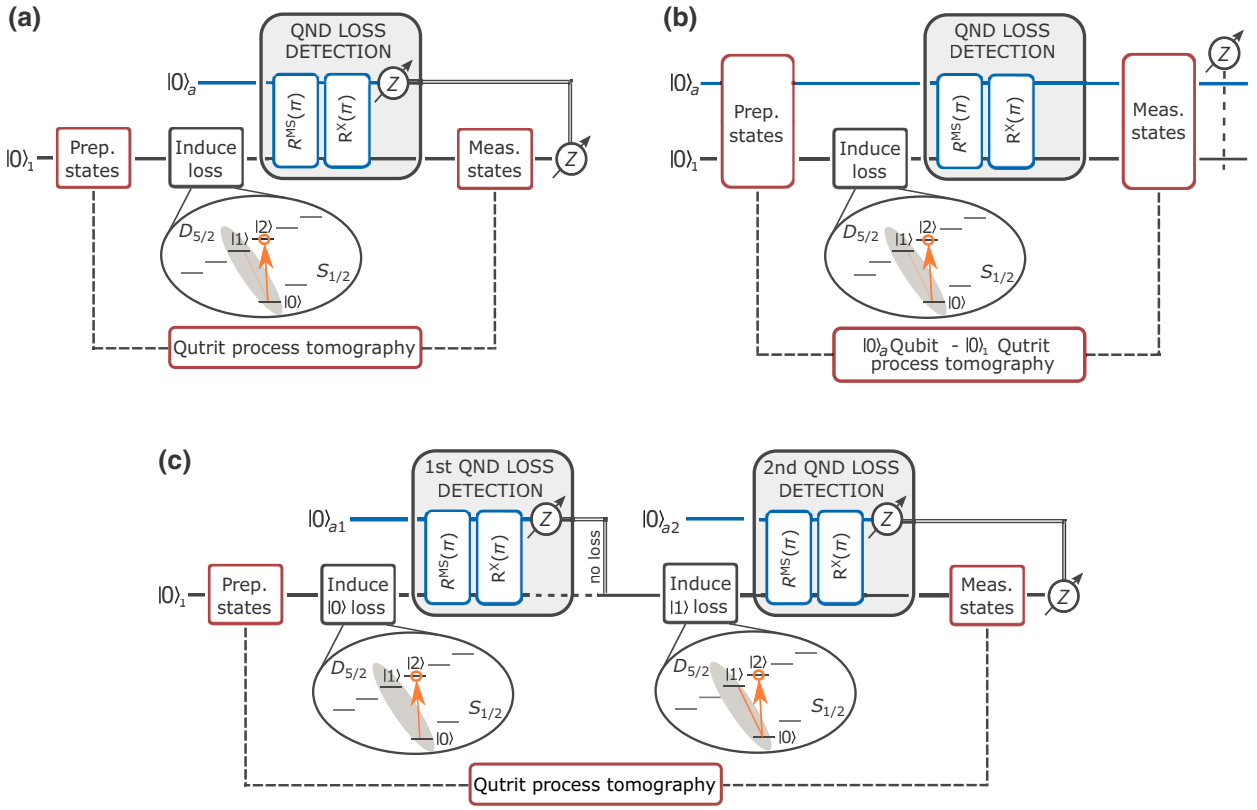

FIG. 16. Schematics on higher-dimensional process tomography. (a) Qutrit process tomography solely covering the system qubit (q) together with the loss level $\{|0\rangle_q, |1\rangle_q, |2\rangle_q\}$ undergoing the QND-detection unit by using nine preparation settings together with six measurement settings, resulting in 54 experiments each run. (b) Combined process tomography on ancilla (a) and qutrit (1), capturing the entire dynamics of this quantum instrument using 12 settings on the ancilla qubit (four preparation settings and three measurement settings) alongside 54 settings on the system qutrit, resulting in 648 experiments. (c) Qutrit process tomography on the erasure channel, focusing on the no-loss case, i.e., twice postselecting the ancilla qubit's $|0\rangle_a$ outcome.

the Bloch sphere towards its center. Note that we implement those models such that they act both on the ancilla and the qutrit using only a single noise parameter [96]. The upper row of Fig. 20 depicts the fidelities (top part) for the individual models at the optimized parameters (bottom part). Both results indicate similar improvements compared to the fidelity with the ideal QND map from Eq. (A5). Numbers on fidelities and optimized parameters for depolarizing noise $p_{\text{depol.}}$ and dephasing noise $p_{\text{deph.}}$ are further summarized in Table I. The parameters typically lie around 1% or below, yet the small increase in fidelity indicates other error mechanisms to be more dominant.

Correlated two-qubit over-rotations.—The erroneous peaks in the experimentally estimated Choi operators from Fig. 15 imply that additional rotations should be taken into account by the agnostic models. Those dominant error peaks are found originating from correlated rotations between the ancilla and system qubit, as illustratively labeled in Fig. 21(a). Note that the error terms are restricted to the qubit level and partial coherences are still present. Hence, if the system qutrit's state is $|2\rangle_q$, no correlated error is induced on the ancilla qubit. Therefore, correlated errors are due to faulty entangling R^{MS} gates. A potential noise model covering correlated rotations in such a way reads

$$\rho \mapsto \mathcal{E}_{\text{noise}}(\rho) = U_{\text{corr}} \rho U_{\text{corr}}^{\dagger} \tag{A14}$$

with

$$U_{\text{corr}} = \cos\frac{\alpha}{2}\, \mathbb{1}_a \otimes \mathbb{1}_q + i \sin\frac{\alpha}{2}\, (X_a \otimes X_q + \mathbb{1}_a \otimes |2\rangle\langle 2|_q), \tag{A15}$$

where α describes the correlated under- and over-rotations and relates to the corresponding error probability via $p_{\text{corr.}} = \sin(\alpha/2)^2$. For comparison, a value $p_{\text{corr.}}$ of 0.5 would induce a maximally entangling two-qubit operation on the ancilla and system qubit. We first test the model alone followed by combining it with depolarizing and dephasing noise. The resulting fidelities (top part) at the optimized model parameters (bottom part) are shown in the second row of Fig. 20 and clearly overcome those on the agnostic models denoting correlated rotations to

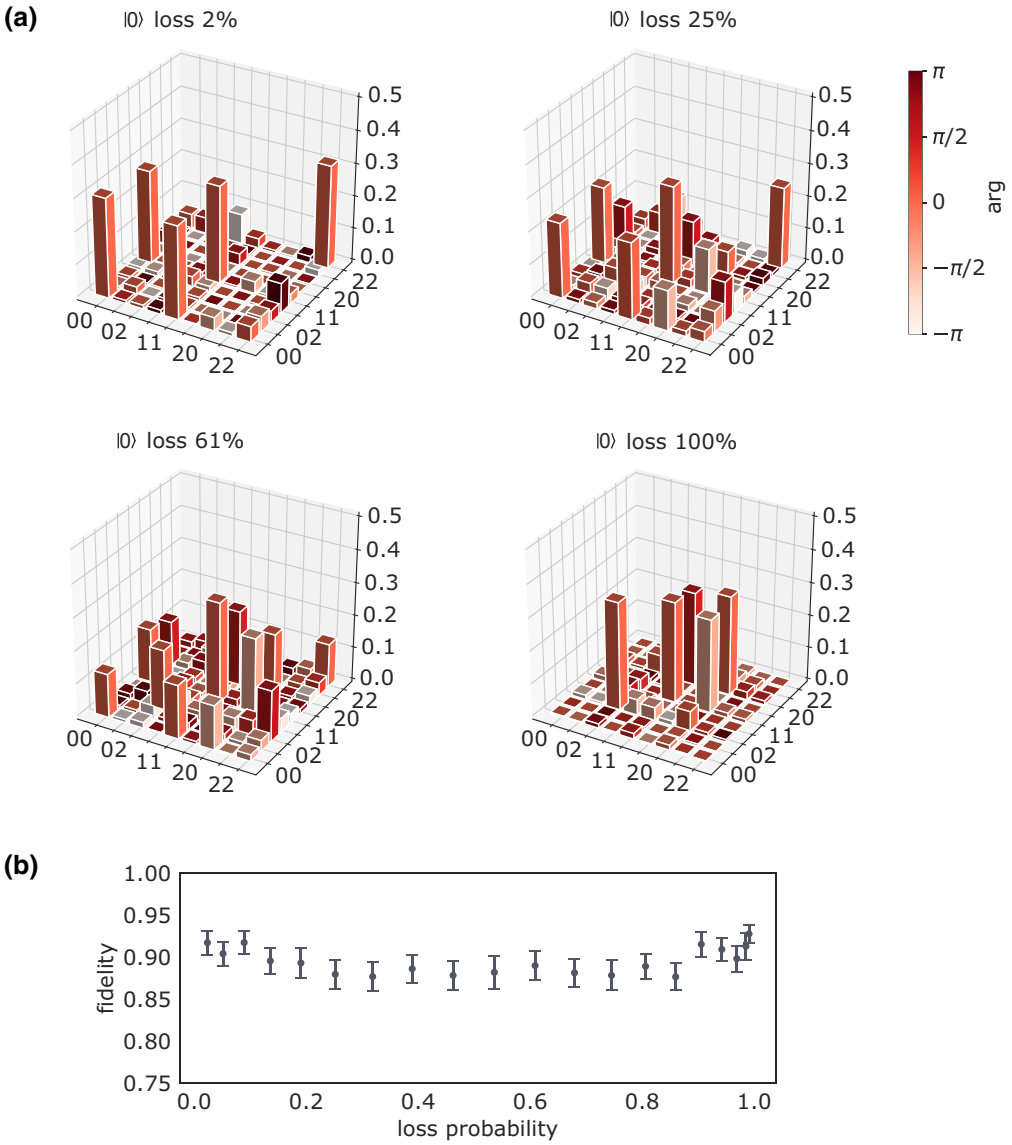

FIG. 17. Qutrit process tomography characterizing the QND-detection unit for loss from $|0\rangle_q$ according to Fig. 16(a). (a) System qutrit's Choi operator in elementary basis $\{|00\rangle_q, \ldots, |22\rangle_q\}$ after tracing over the ancilla qubit and various loss probabilities denoting the effect of the loss transition transferring population from $|0\rangle_q$ to $|2\rangle_q$. (b) The respective fidelities with the ideal Choi operators covering the complete loss range.

be our leading noise mechanism. The effect of the additional depolarizing and dephasing noise (bottom right) leads to slight improvements. The modeled Choi operator on this combined noise model is plotted for the no-loss case in Fig. 21(b), showing strong similarities to the experimental one and underlining good agreement between the model and experiment. Numbers on fidelities and optimized parameters for all models are summarized in Table I.

Correlated and single over-rotations.—Finally, we combine the action of correlated rotations with single-qubit rotations on the ancilla and the qutrit and we consider the coherent error model given by

$$\rho \mapsto \mathcal{E}_{\text{noise}}(\rho) = R\, U_{\text{corr}} \rho U_{\text{corr}}^{\dagger} R^{\dagger}, \tag{A16}$$

where ρ is the state obtained after the application of the loss operation U of Eq. (A5) [see also Fig. 8(a) of the main text], U_{corr} is a correlated two-qubit over-rotation defined in Eq. (A15), and $R = R_a^X(\beta) R_q^X(\beta)$ with

$$R_a^X(\beta) = \cos(\beta/2)\mathbb{1}_a - i\sin(\beta/2)X_a, \tag{A17}$$

$$R_q^X(\beta) = \cos(\beta/2)(\mathbb{1}_q - |2\rangle\langle 2|_q) - i\sin(\beta/2)X_q + |2\rangle\langle 2|_q \tag{A18}$$

over-rotations with angle β of the ancilla and the qutrit system that corresponds to the single-qubit flip error rate $p_{\text{single}} = \sin(\beta/2)^2$. After measurement of the ancilla, the quantum process arising from the erroneous channel in Eq. (A16) can be written as

$$\rho \mapsto |0\rangle\langle 0|_a \otimes \mathcal{R}_0(\rho_q) + |1\rangle\langle 1|_a \otimes \mathcal{R}_1(\rho_q), \tag{A19}$$

where ρ_q is the state related to the qutrit only and the processes $\mathcal{R}_0$ and $\mathcal{R}_1$ describe the maps that transform the

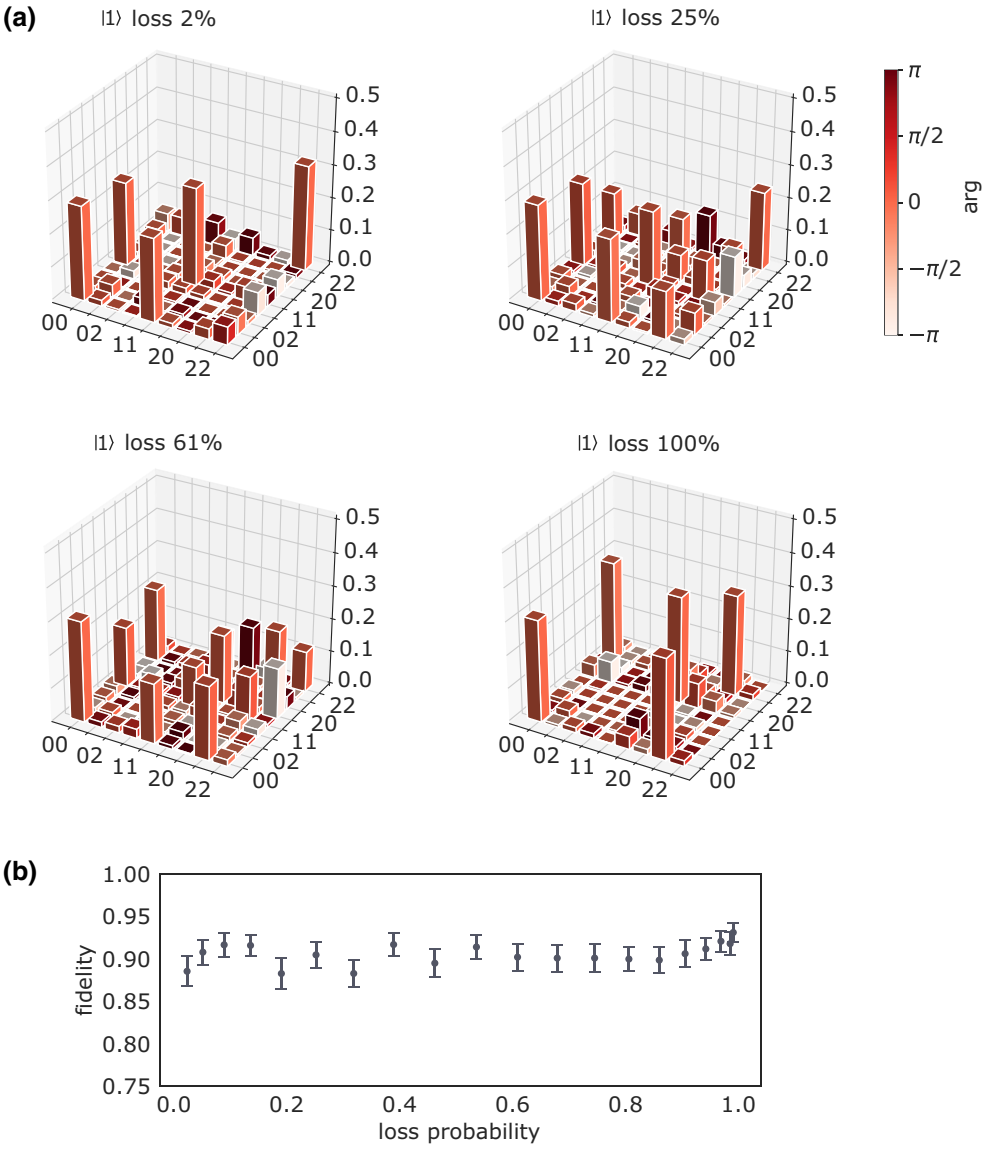

FIG. 18. Qutrit process tomography characterizing the QND-detection unit for loss from $|1\rangle_q$ according to Fig. 16(a). (a) System qutrit's Choi operator in elementary basis $\{|00\rangle_q, \ldots, |22\rangle_q\}$ after tracing over the ancilla qubit and several different loss probabilities denoting the effect of the loss transition transferring population from $|1\rangle_q$ to $|2\rangle_q$. (b) The respective fidelities compared to the ideal Choi operators covering the complete loss range.

qutrit state in the case of no-loss detected (ancilla qubit in $|0\rangle_a$) and of loss detected (ancilla qubit in $|1\rangle_a$). The Choi operators Λ_0 and Λ_1 of maps $\mathcal{R}_0$ and $\mathcal{R}_1$ can be computed for all values of the over-rotated angles α and β. In particular, if we consider small deviations for α and β, Λ_0 and Λ_1 read at second order

$$\Lambda_0 = \begin{pmatrix}
1-\frac{\alpha^2}{4}-\frac{\beta^2}{2} & \left(-\frac{\alpha}{4}-\frac{i}{2}\right)\beta & 0 & \left(-\frac{\alpha}{4}-\frac{i}{2}\right)\beta & 1-\frac{\alpha^2}{4}-\frac{\beta^2}{2} & 0 & 0 & 0 & \frac{i}{2}\beta \\
\left(-\frac{\alpha}{4}+\frac{i}{2}\right)\beta & \frac{\beta^2}{4} & 0 & \frac{\beta^2}{4} & \left(-\frac{\alpha}{4}+\frac{i}{2}\right)\beta & 0 & 0 & 0 & -\frac{1}{4}\beta^2 \\
0 & 0 & 0 & 0 & 0 & 0 & 0 & 0 & 0 \\
\left(-\frac{\alpha}{4}+\frac{i}{2}\right)\beta & \frac{\beta^2}{4} & 0 & \frac{\beta^2}{4} & \left(-\frac{\alpha}{4}+\frac{i}{2}\right)\beta & 0 & 0 & 0 & -\frac{1}{4}\beta^2 \\
1-\frac{\alpha^2}{4}-\frac{\beta^2}{2} & \left(-\frac{\alpha}{4}-\frac{i}{2}\right)\beta & 0 & \left(-\frac{\alpha}{4}-\frac{i}{2}\right)\beta & 1-\frac{\alpha^2}{4}-\frac{\beta^2}{2} & 0 & 0 & 0 & \frac{i}{2}\beta \\
0 & 0 & 0 & 0 & 0 & 0 & 0 & 0 & 0 \\
0 & 0 & 0 & 0 & 0 & 0 & 0 & 0 & 0 \\
0 & 0 & 0 & 0 & 0 & 0 & 0 & 0 & 0 \\
-\frac{i}{2}\beta & -\frac{1}{4}\beta^2 & 0 & -\frac{1}{4}\beta^2 & -\frac{i}{2}\beta & 0 & 0 & 0 & \frac{\beta^2}{4}
\end{pmatrix}, \tag{A20}$$

$$\Lambda_1 = \begin{pmatrix} \frac{\beta^2}{4} & \frac{\alpha\beta}{4} & 0 & \frac{\alpha\beta}{4} & \frac{\beta^2}{4} & 0 & 0 & 0 & \left(\frac{\alpha}{4} - \frac{i}{2}\right)\beta \\ \frac{\alpha\beta}{4} & \frac{\alpha^2}{4} & 0 & \frac{\alpha^2}{4} & \frac{\alpha\beta}{4} & 0 & 0 & 0 & \frac{\beta^2}{4} - \frac{i\alpha}{2} \\ 0 & 0 & 0 & 0 & 0 & 0 & 0 & 0 & 0 \\ \frac{\alpha\beta}{4} & \frac{\alpha^2}{4} & 0 & \frac{\alpha^2}{4} & \frac{\alpha\beta}{4} & 0 & 0 & 0 & \frac{\beta^2}{4} - \frac{i\alpha}{2} \\ \frac{\beta^2}{4} & \frac{\alpha\beta}{4} & 0 & \frac{\alpha\beta}{4} & \frac{\beta^2}{4} & 0 & 0 & 0 & \left(\frac{\alpha}{4} - \frac{i}{2}\right)\beta \\ 0 & 0 & 0 & 0 & 0 & 0 & 0 & 0 & 0 \\ 0 & 0 & 0 & 0 & 0 & 0 & 0 & 0 & 0 \\ 0 & 0 & 0 & 0 & 0 & 0 & 0 & 0 & 0 \\ \left(\frac{\alpha}{4} + \frac{i}{2}\right)\beta & \frac{\beta^2}{4} + \frac{i\alpha}{2} & 0 & \frac{\beta^2}{4} + \frac{i\alpha}{2} & \left(\frac{\alpha}{4} + \frac{i}{2}\right)\beta & 0 & 0 & 0 & 1 - \frac{\beta^2}{4} \end{pmatrix}, \tag{A21}$$

where we have labeled the qutrit basis states in the order $|00\rangle, |01\rangle, |02\rangle, \ldots, |22\rangle$. In the next section we discuss how to approximate the channel in Eq. (A19) with Clifford gates.

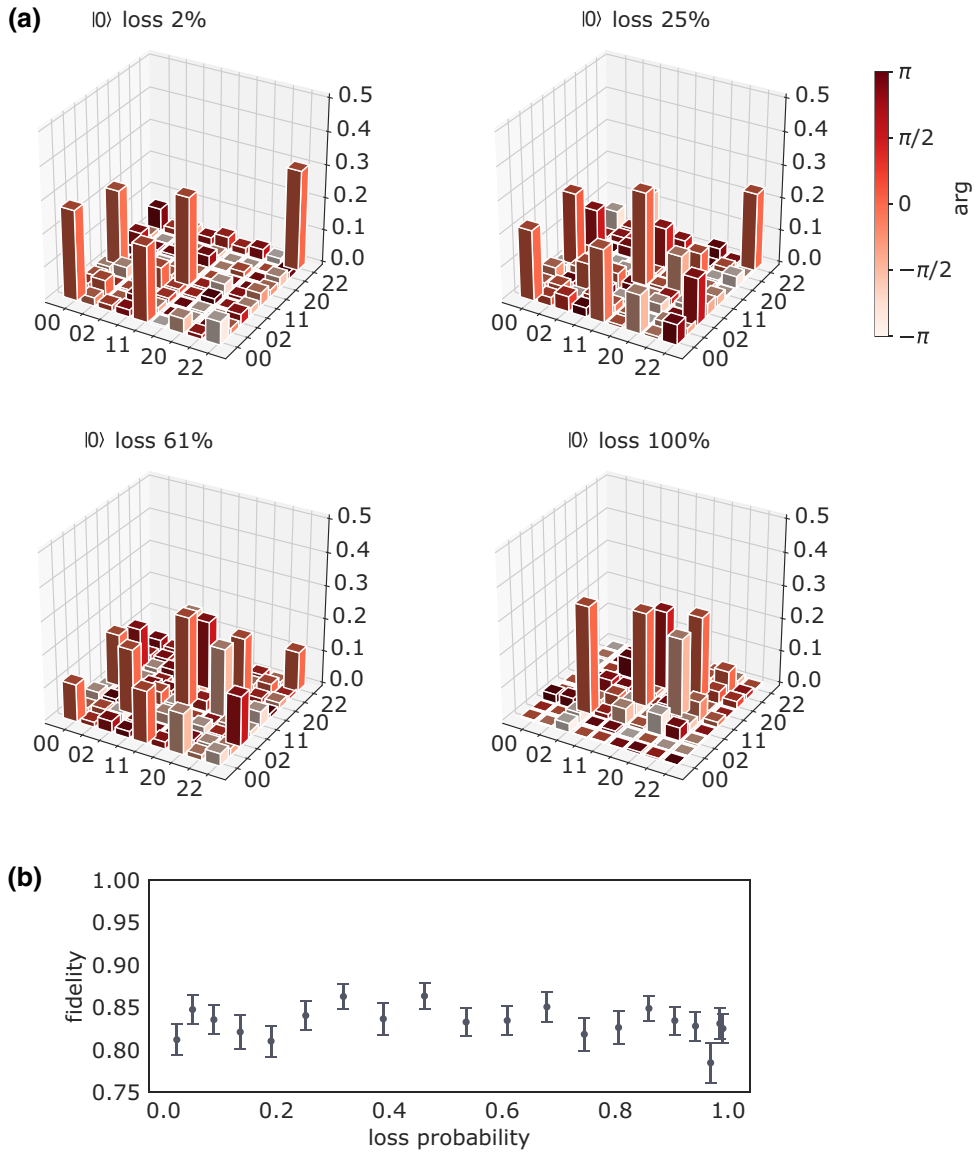

FIG. 19. Qutrit process tomography on two repeated QND detections for loss from $|0\rangle_q$ according to Fig. 16(a). (a) System qutrit Choi operators mapping loss repeatedly onto ancillae a_1 and a_2 under several different loss probabilities. The processes for which we trace over both ancillae prior to reconstruction denote the loss transition transferring population from $|0\rangle_q$ to $|2\rangle_q$. (b) Fidelities compared to the ideal operators remain approximately constant along all measured loss probabilities and show slightly decreased values compared to the results on single QND detection from Fig. 17.

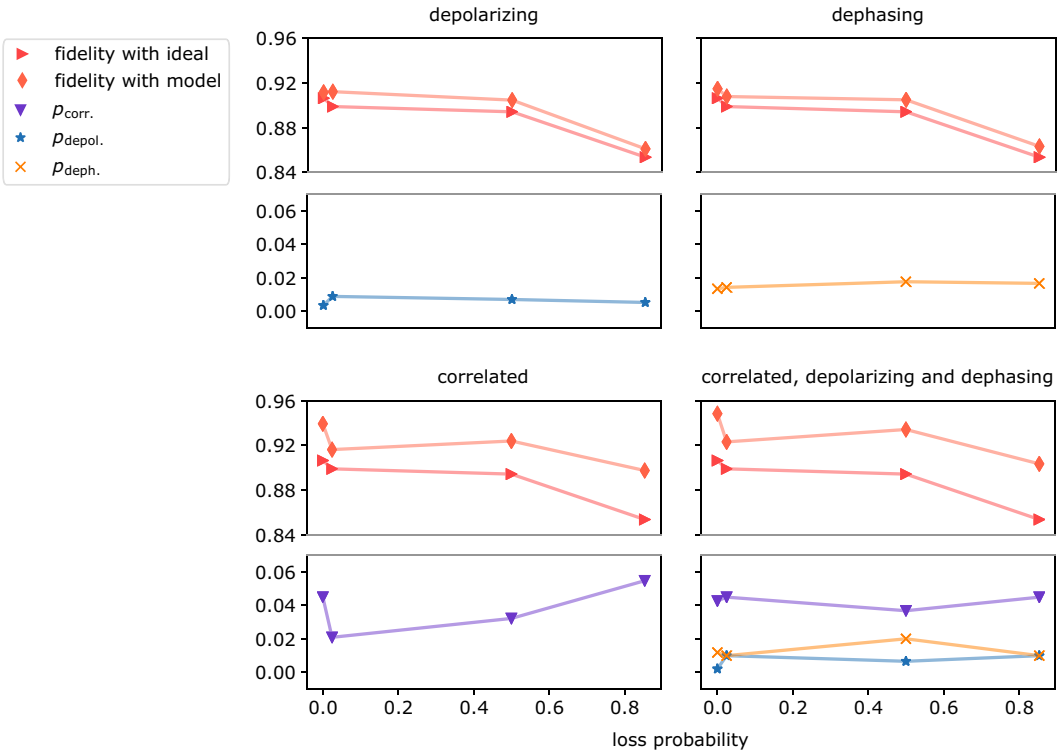

FIG. 20. Noise-model QND detection. Various noise model describing the experimental limitations on the ancilla-qutrit Choi operator depicted in Fig. 15. The limitations are best described when combining correlated coherent rotations together with depolarizing and dephasing noise. Correlated errors clearly dominate as depolarizing and dephasing errors only lead to minor improvements. The error parameters on the bottom of each plot refer to depolarizing error $p_{\text{depol.}}$, dephasing error $p_{\text{deph.}}$, and correlated error $p_{\text{corr.}}$, the latter according to Eq. (A15). Lines connect the points for clarity.

Effective Clifford channel.—Before deriving the analytical expression for the Clifford channel, the forms of Choi operators Λ_0 and Λ_1 allow us to have a qualitative discussion on the events that will form the Clifford channel approximating Eq. (A19). In Λ_0 and Λ_1 we can easily identify the following events happening to the ancilla-qutrit system. If the ancilla is in $|0\rangle_a$, the qutrit state is left unchanged with probability $1-\alpha^2/4-\beta^2/2$ or it undergoes an X_q bit-flip error with probability $\beta^2/4$. When the ancilla is instead in $|1\rangle_a$, the qutrit state is left unchanged in the loss state $|2\rangle\langle 2|_q$ with probability $1-\beta^2/4$.

We can also identify the origin of the false-negative and false-positive events. From Λ_0 we see that the qutrit will be projected on the loss state $|2\rangle\langle 2|_q$ with probability $\beta^2/4$, while the ancilla will be in the no-loss detected state $|0\rangle_a$. This corresponds to a false-negative event whose origin can be traced back to the single-qubit over-rotation R of Eq. (A16).

From Λ_1 we see that, when the qutrit is generated in the computational space by $|0\rangle_q$ and $|1\rangle_q$, the ancilla will be found in the loss detected state $|1\rangle_a$. In particular, the qutrit will be left unchanged with probability $\beta^2/4$ and it will undergo an X_q bit-flip error with probability $\alpha^2/4$. These events correspond to false-positive events whose origin can be traced back to the single-qubit over-rotation R and to the correlated over-rotation U_{corr} of Eq. (A16).

TABLE I. Summary on noise model parameters and results. The parameters and fidelities refer to the best suitable model values describing the experimental noise from Fig. 20: depolarizing error $p_{\text{depol.}}$, dephasing error $p_{\text{deph.}}$, and correlated error $p_{\text{corr.}}$ according to Eq. (A15).

Loss		Depolarizing		Dephasing		Correlated		Correlated, depol., and deph.			
(%)	F_{ideal}	$\mathcal{F}_{\text{model}}$	$p_{\text{depol.}}$	$\mathcal{F}_{\text{model}}$	$p_{\text{deph.}}$	$\mathcal{F}_{\text{model}}$	$p_{\text{corr.}}$	$\mathcal{F}_{\text{model}}$	$p_{\text{corr.}}$	$p_{\text{depol.}}$	$p_{\text{deph.}}$
0	0.906	0.912	0.004	0.915	0.013	0.939	0.045	0.948	0.042	0.012	0.002
2	0.899	0.912	0.009	0.908	0.014	0.916	0.021	0.923	0.045	0.010	0.010
50	0.894	0.905	0.007	0.905	0.018	0.924	0.032	0.934	0.037	0.020	0.007
85	0.854	0.861	0.005	0.863	0.017	0.897	0.054	0.903	0.045	0.010	0.010

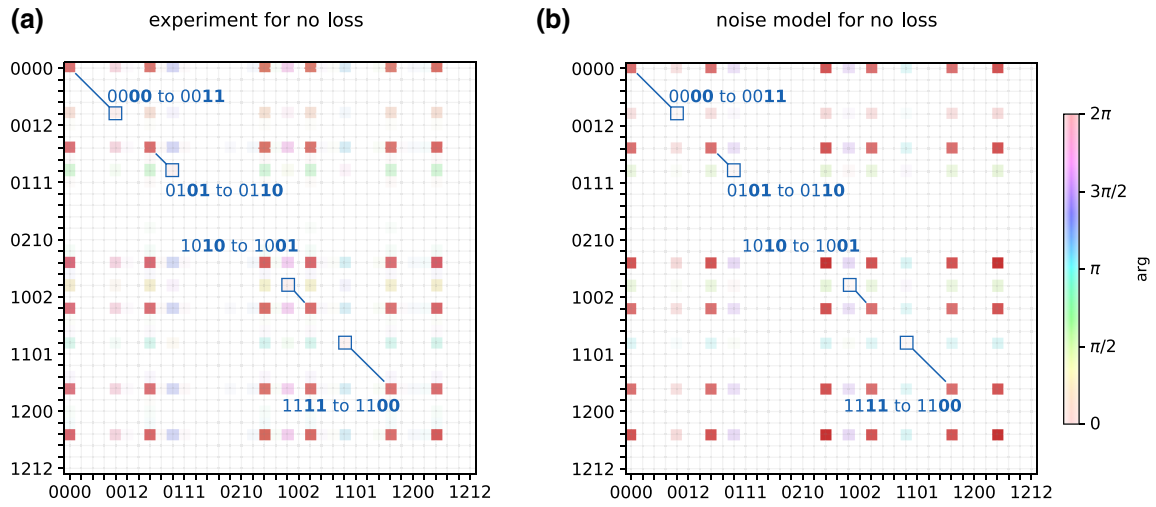

FIG. 21. Comparison between experimental and noisy-modeled Choi operators. (a) Experimentally estimated map according to Fig. 15(a) with additionally marked transitions denoting correlated errors describing our leading error mechanism; see Eq. (A15). (b) Most suitable noisy-modeled Choi operator combining correlated, depolarizing, and dephasing errors.

The previous considerations on the Choi operators Λ_0 and Λ_1 can be made more precise by explicitly computing the process in Eq. (A19) with the help of Eqs. (A15), (A17), and (A18) and by retaining only the terms that can be written in the Kraus form $P\rho P^\dagger$, where P is a Pauli operator. In this way, we can approximate the channel in Eq. (A19) as

$$\begin{aligned}\rho \mapsto\ & p_a P_{01}\rho P_{01}^\dagger + p_b X_q\rho X_q + p_c X_a X_q \rho X_q X_a \\ & + p_d X_a P_{01}\rho P_{01}^\dagger X_a + q_a X_a\,|2\rangle\langle 2|\,\rho\,|2\rangle\langle 2|\,X_a \\ & + q_b\,|2\rangle\langle 2|\,\rho\,|2\rangle\langle 2|\,, \end{aligned} \tag{A22}$$

where ρ is the density matrix of the whole ancilla and qutrit system, $P_{01} = 1 - |2\rangle\langle 2|_q$ is the projector on the computational space $\{|0\rangle_q, |1\rangle_q\}$ of the qutrit, and the probabilities take the form

$$p_a = \sin^2\alpha \sin^4\beta + \cos^2\alpha\cos^4\beta \sim 1 - \alpha^2/4 - \beta^2/2, \tag{A23}$$

$$p_b = \sin^2\beta/4 \sim \beta^2/4, \tag{A24}$$

$$p_c = \sin^2\alpha\cos^4\beta + \cos^2\alpha\sin^4\beta \sim \alpha^2/4, \tag{A25}$$

$$p_d = \sin^2\beta/4 \sim \beta^2/4, \tag{A26}$$

$$q_a = \cos^2(\beta/2) \sim 1 - \beta^2/4, \tag{A27}$$

$$q_b = \sin^2(\beta/2) \sim \beta^2/4. \tag{A28}$$

The channel in Eq. (A22) can then be implemented in the following way.

1. If the ancilla is in $|0\rangle_a$, we
   (a) leave the qutrit state in the computational space with probability $1 - \beta^2/2 - \alpha^2/4$;
   (b) apply an X_q bit-flip error to the qutrit with probability $\beta^2/4$;
   (c) apply an X_q bit-flip error to the qutrit and an X_a bit-flip error to the ancilla with probability $\alpha^2/4$ (corresponding to a false-positive event from the correlated over-rotation);
   (d) leave the qutrit state as it is and flip the ancilla with probability $\beta^2/4$ (corresponding to a false-positive event from the single rotations).
2. If the ancilla is in $|1\rangle_a$, we
   (a) leave the qutrit state in the loss state $|2\rangle_q$ with probability $1 - \beta^2/4$;
   (b) flip the ancilla to the no-loss detection state $|0\rangle_a$ with probability $\beta^2/4$ (corresponding to a false-negative from the single rotations).

The comparison between the coherent channel in Eq. (A16) and the effective Clifford channel previously described is shown in Fig. 22 and in Fig. 10 of the main text.

3. Losses in the seven-qubit code

In this section, we discuss the correction from losses for the seven-qubit color code, in the ideal scenario of perfect QND loss detection and stabilizer measurements. We also assume that losses occur on each qubit independently with loss probability p.

A loss event is correctable if the density matrix of the losses is fully mixed or, more generally, it does not contain any information on the encoded logical state. With this criterion, we can then check the loss events that can be corrected. Obviously, the event [happening with probability

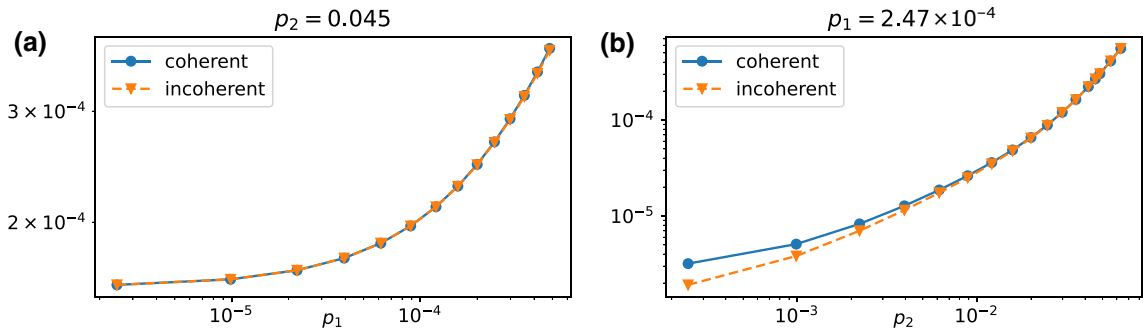

FIG. 22. Comparison between the coherent and incoherent implementations of the faulty QND loss detection unit in the case of no losses. (a) Logical error rate as a function of the correlated over-rotation rate p_1 for the parameter $p_2 = 0.045$ obtained from the experimental data. (b) Logical error rate as a function of the correlated over-rotation rate p_2 for the parameter $p_1 = 2.47 \times 10^{-4}$ obtained from the experimental model.

$P_0 = (1-p)^7]$ where no loss occurs is correctable. The events where one loss occurs are also correctable. To show this, let us consider, for instance, the encoded $|0_L\rangle$ state

$$|0_L\rangle \sim (\mathbb{1} + S_x^{(1)})(\mathbb{1} + S_x^{(2)})(\mathbb{1} + S_x^{(3)})\,|0\rangle^{\otimes 7}\,, \tag{A29}$$

where the $S_x^{(j)}$ are the stabilizer generators, and let us suppose that the loss affects qubit q_1 [see Fig. 8(a) of the main text]. By introducing the two orthogonal states $|\chi_0\rangle = P_x^{(2)}P_x^{(3)}\,|0\rangle^{\otimes 6}$ and $|\chi_1\rangle = X_2X_3X_4P_x^{(2)}P_x^{(3)}\,|0\rangle^{\otimes 6}$ (where $P_x^{(j)} = \mathbb{1} + S_x^{(j)}$ with $j = 2, 3$ are chosen because the loss does not belong to $S_x^{(j)}$), the state $|0_L\rangle$ can be written explicitly as

$$|0_L\rangle \sim |0_1\rangle\,|\chi_0\rangle + |1_1\rangle\,|\chi_1\rangle\,. \tag{A30}$$

As $|\chi_0\rangle$ and $|\chi_1\rangle$ are orthogonal, the reduced density matrix of the loss q_1 obtained by tracing out the six other qubits will be $\rho_1 \sim |0_1\rangle\langle 0_1| + |1_1\rangle\langle 1_1|$, i.e., it will be fully mixed. Therefore, the events with one loss [happening with probability $P_1 = 7p(1-p)^6$] can be correctable. A similar reasoning applies to all the events where two losses happen [$P_2 = 21p^2(1-p)^5$] and to the events where three losses that do not form a logical operator happen as well. The events with three losses that form a logical operator are instead not correctable. There are precisely seven such events [corresponding to the logical operators $\mathcal{L} = \{[1,2,5], [1,3,6], [1,4,7], [2,3,7], [4,3,5], [5,6,7], [2,4,6]\}$ in Fig. 8(a) of the main text]. The last one ([2, 4, 6]) is given by the product of the logical operator acting on all the seven qubits multiplied by all three stabilizer generators. This implies that the probability to successfully recover the logical state is $P_3 = [\binom{7}{3} - 7]p^3(1-p)^4 = 28p^3(1-p)^4$. In the case of four losses, in seven cases out of $\binom{7}{4} = 35$, the reduced density matrix of the losses does not depend on the encoded logical state. These cases correspond to the losses happening on the qubits of the stabilizer generators and their products and are given by

$$\begin{aligned}\mathcal{S} = \{&[1,2,3,4], [2,3,5,6], [3,4,6,7], [1,4,5,6],\\ &[1,2,6,7], [2,4,5,7], [1,3,5,7]\}.\end{aligned} \tag{A31}$$

This can be shown by considering, for instance, four losses happening on the stabilizer [1, 2, 3, 4]. A bit of algebra shows that the logical states $|0_L\rangle$ and $|1_L\rangle$ can be written as

$$\begin{aligned}|0_L\rangle = {}&|G\rangle\,|000\rangle + X_2X_3\,|G\rangle\,|110\rangle + X_3X_4\,|G\rangle\,|011\rangle\\ &+ X_2X_4\,|G\rangle\,|101\rangle\,,\end{aligned} \tag{A32}$$

$$\begin{aligned}|1_L\rangle = {}&|G\rangle\,|111\rangle + X_2X_3\,|G\rangle\,|001\rangle + X_3X_4\,|G\rangle\,|100\rangle\\ &+ X_2X_4\,|G\rangle\,|010\rangle\,,\end{aligned} \tag{A33}$$

where $|G\rangle = |0000\rangle + |1111\rangle$ is a GHZ state of qubits 1, 2, 3, 4 where the losses happen. Tracing on qubits 5, 6, 7 transforms any logical state $|\psi_L\rangle = c_0\,|0_L\rangle + c_1\,|1_L\rangle$ into a mixture with equal probabilities of the four states $\{|G\rangle, X_2X_3\,|G\rangle, X_3X_4\,|G\rangle, X_2X_4\,|G\rangle\}$ that is independent on the coefficients c_0 and c_1. Finally, no event with five, six, or seven losses can be corrected. The total probability of a successful correction is given by the sum of all probabilities P_j and reads

$$\begin{aligned}p_{\text{success}} &= (1-p)^7 + 7p(1-p)^6 + 21p^2(1-p)^5\\ &\quad + 28p^3(1-p)^4 + 7p^4(1-p)^3\\ &= 1 - 7p^3 + 21p^5 - 21p^6 + 6p^7.\end{aligned} \tag{A34}$$

[1] D. Gottesman, Theory of fault-tolerant quantum computation, Phys. Rev. A **57**, 127 (1998).

[2] P. Schindler, J. T. Barreiro, T. Monz, V. Nebendahl, D. Nigg, M. Chwalla, M. Hennrich, and R. Blatt, Experimental repetitive quantum error correction, Science **332**, 1059 (2011).

[3] L. Sun, A. Petrenko, Z. Leghtas, B. Vlastakis, G. Kirchmair, K. M. Sliwa, A. Narla, M. Hatridge, S. Shankar, J. Blumoff, L. Frunzio, M. Mirrahimi, M. H. Devoret, and R. J. Schoelkopf, Tracking photon jumps with repeated quantum non-demolition parity measurements, Nature **511**, 444 (2014).

[4] J. Kelly *et al.*, State preservation by repetitive error detection in a superconducting quantum circuit, Nature **519**, 66 (2015).

[5] J. Cramer, N. Kalb, M. A. Rol, B. Hensen, M. S. Blok, M. Markham, D. J. Twitchen, R. Hanson, and T. H. Taminiau, *Repeated quantum error correction on a continuously encoded qubit by real-time feedback*, Nat. Commun. **7**, 11526 (2016).

[6] T. Unden, P. Balasubramanian, D. Louzon, Y. Vinkler, M. B. Plenio, M. Markham, D. Twitchen, A. Stacey, I. Lovchinsky, A. O. Sushkov, M. D. Lukin, A. Retzker, B. Naydenov, L. P. McGuinness, and F. Jelezko, Quantum Metrology Enhanced by Repetitive Quantum Error Correction, Phys. Rev. Lett. **116**, 230502 (2016).

[7] V. Negnevitsky, M. Marinelli, K. K. Mehta, H.-Y. Lo, C. Flühmann, and J. P. Home, Repeated multi-qubit readout and feedback with a mixed-species trapped-ion register, Nature **563**, 527 (2018).

[8] T. Monz, D. Nigg, E. A. Martinez, M. F. Brandl, P. Schindler, R. Rines, S. X. Wang, I. L. Chuang, and R. Blatt, Realization of a scalable Shor algorithm, Science **351**, 1068 (2016).

[9] A. Y. Kitaev, Quantum measurements and the Abelian stabilizer problem, Electron. Colloquium Comput. Complex. **3** (1996).

[10] R. Jozsa, *Quantum Information Processing* (2005), Vol. 199, p. 137.

[11] R. Stricker, D. Vodola, A. Erhard, L. Postler, M. Meth, M. Ringbauer, P. Schindler, T. Monz, M. Müller, and R. Blatt, Experimental deterministic correction of qubit loss, Nature **585**, 207 (2020).

[12] C. Unnikrishnan, Quantum non-demolition measurements: Concepts, theory and practice, Curr. Sci. **109**, 2052 (2015).

[13] D. B. Hume, T. Rosenband, and D. J. Wineland, High-Fidelity Adaptive Qubit Detection through Repetitive Quantum Nondemolition Measurements, Phys. Rev. Lett. **99**, 120502 (2007).

[14] C. Sayrin, I. Dotsenko, X. Zhou, B. Peaudecerf, T. Rybarczyk, S. Gleyzes, P. Rouchon, M. Mirrahimi, H. Amini, M. Brune, J.-M. Raimond, and S. Haroche, Real-time quantum feedback prepares and stabilizes photon number states, Nature **477**, 73 (2011).

[15] M. Hatridge, S. Shankar, M. Mirrahimi, F. Schackert, K. Geerlings, T. Brecht, K. M. Sliwa, B. Abdo, L. Frunzio, S. M. Girvin, R. J. Schoelkopf, and M. H. Devoret, Quantum back-action of an individual variable-strength measurement, Science **339**, 178 (2013).

[16] M. S. Blok, C. Bonato, M. L. Markham, D. J. Twitchen, V. V. Dobrovitski, and R. Hanson, Manipulating a qubit through the backaction of sequential partial measurements and real-time feedback, Nat. Phys. **10**, 189 (2014).

[17] K. Rudinger, G. J. Ribeill, L. C. G. Govia, M. Ware, E. Nielsen, K. Young, T. A. Ohki, R. Blume-Kohout, and T. Proctor, Characterizing mid-circuit measurements on a superconducting qubit using gate set tomography, Phys. Rev. Appl. **17**, 014014 (2022).

[18] H.-P. Breuer and F. Petruccione, *The Theory of Open Quantum Systems* (Oxford University Press, 2006).

[19] M. Ringbauer, C. J. Wood, K. Modi, A. Gilchrist, A. G. White, and A. Fedrizzi, Characterizing Quantum Dynamics with Initial System-Environment Correlations, Phys. Rev. Lett. **114**, 090402 (2015).

[20] I. Rotter and J. P. Bird, A review of progress in the physics of open quantum systems: Theory and experiment, Rep. Prog. Phys. **78**, 114001 (2015).

[21] J. T. Barreiro, M. Müller, P. Schindler, D. Nigg, T. Monz, M. Chwalla, M. Hennrich, C. F. Roos, P. Zoller, and R. Blatt, An open-system quantum simulator with trapped ions, Nature **470**, 486 (2011).

[22] P. Schindler, M. Müller, D. Nigg, J. T. Barreiro, E. A. Martinez, M. Hennrich, T. Monz, S. Diehl, P. Zoller, and R. Blatt, Quantum simulation of dynamical maps with trapped ions, Nat. Phys. **9**, 361 (2013).

[23] M. Müller, K. Hammerer, Y. L. Zhou, C. F. Roos, and P. Zoller, Simulating open quantum systems: From many-body interactions to stabilizer pumping, New J. Phys. **13**, 085007 (2011).

[24] L. M. Sieberer, M. Buchhold, and S. Diehl, Keldysh field theory for driven open quantum systems, Rep. Prog. Phys. **79**, 096001 (2016).

[25] E. B. Davies and J. T. Lewis, An operational approach to quantum probability, Commun. Math. Phys. **17**, 239 (1970).

[26] M. Ozawa, Quantum measuring processes of continuous observables, J. Math. Phys. **25**, 79 (1984).

[27] J. Dressel and A. N. Jordan, Quantum instruments as a foundation for both states and observables, Phys. Rev. A **88**, 022107 (2013).

[28] G. Chiribella, G. M. D'Ariano, and P. Perinotti, Theoretical framework for quantum networks, Phys. Rev. A **80**, 022339 (2009).

[29] O. Oreshkov, F. Costa, and Č. Brukner, Quantum correlations with no causal order, Nat. Commun. **3**, 1092 (2012).

[30] F. Buscemi and M. F. Sacchi, Information-disturbance trade-off in quantum-state discrimination, Phys. Rev. A **74**, 052320 (2006).

[31] L. Knips, J. Dziewior, A.-L. K. Hashagen, J. D. A. Meinecke, H. Weinfurter, and M. M. Wolf, Measurement-disturbance tradeoff outperforming optimal cloning, arXiv: preprint:1808.07882 (2018).

[32] S. Lloyd and J.-J. E. Slotine, Quantum feedback with weak measurements, Phys. Rev. A **62**, 012307 (2000).

[33] Q. Sun, M. Al-Amri, L. Davidovich, and M. S. Zubairy, Reversing entanglement change by a weak measurement, Phys. Rev. A **82**, 052323 (2010).

[34] Y.-S. Kim, J.-C. Lee, O. Kwon, and Y.-H. Kim, Protecting entanglement from decoherence using weak measurement and quantum measurement reversal, Nat. Phys. **8**, 117 (2012).

[35] S. Wagner, J.-D. Bancal, N. Sangouard, and P. Sekatski, Device-independent characterization of quantum instruments, Quantum **4**, 243 (2020).

[36] N. Miklin, J. J. Borkała, and M. Pawłowski, Semi-device-independent self-testing of unsharp measurements, Phys. Rev. Res. **2**, 033014 (2020).

[37] K. Mohan, A. Tavakoli, and N. Brunner, Sequential random access codes and self-testing of quantum measurement instruments, New J. Phys. **21**, 083034 (2019).

[38] E. S. Gómez, S. Gómez, P. González, G. Cañas, J. F. Barra, A. Delgado, G. B. Xavier, A. Cabello, M. Kleinmann, T. Vértesi, and G. Lima, Device-Independent Certification of a Nonprojective Qubit Measurement, Phys. Rev. Lett. **117**, 260401 (2016).

[39] M. Smania, P. Mironowicz, M. Nawareg, M. Pawłowski, A. Cabello, and M. Bourennane, Experimental certification of an informationally complete quantum measurement in a device-independent protocol, Optica **7**, 123 (2020).

[40] J. Helsen, I. Roth, E. Onorati, A. H. Werner, and J. Eisert, A general framework for randomized benchmarking, arXiv:2010.07974 (2020).

[41] E. Knill, D. Leibfried, R. Reichle, J. Britton, R. B. Blakestad, J. D. Jost, C. Langer, R. Ozeri, S. Seidelin, and D. J. Wineland, Randomized benchmarking of quantum gates, Phys. Rev. A **77**, 012307 (2008).

[42] J. P. Gaebler, T. R. Tan, Y. Lin, Y. Wan, R. Bowler, A. C. Keith, S. Glancy, K. Coakley, E. Knill, D. Leibfried, and D. J. Wineland, High-Fidelity Universal Gate Set for $^{9}Be^{+}$ Ion Qubits, Phys. Rev. Lett. **117**, 060505 (2016).

[43] R. Blume-Kohout, J. K. Gamble, E. Nielsen, K. Rudinger, J. Mizrahi, K. Fortier, and P. Maunz, Demonstration of qubit operations below a rigorous fault tolerance threshold with gate set tomography, Nat. Commun. **8**, 14485 (2017).

[44] A. Erhard, J. J. Wallman, L. Postler, M. Meth, R. Stricker, E. A. Martinez, P. Schindler, T. Monz, J. Emerson, and R. Blatt, Characterizing large-scale quantum computers via cycle benchmarking, Nat. Commun. **10**, 5347 (2019).

[45] D. C. McKay, S. Sheldon, J. A. Smolin, J. M. Chow, and J. M. Gambetta, Three-Qubit Randomized Benchmarking, Phys. Rev. Lett. **122**, 200502 (2019).

[46] A. C. Hughes, V. M. Schäfer, K. Thirumalai, D. P. Nadlinger, S. R. Woodrow, D. M. Lucas, and C. J. Ballance, Benchmarking a High-Fidelity Mixed-Species Entangling Gate, Phys. Rev. Lett. **125**, 080504 (2020).

[47] A. G. Fowler, Coping with qubit leakage in topological codes, Phys. Rev. A **88**, 042308 (2013).

[48] J. Ghosh, A. G. Fowler, J. M. Martinis, and M. R. Geller, Understanding the effects of leakage in superconducting quantum-error-detection circuits, Phys. Rev. A **88**, 062329 (2013).

[49] T. M. Stace, S. D. Barrett, and A. C. Doherty, Thresholds for Topological Codes in the Presence of Loss, Phys. Rev. Lett. **102**, 200501 (2009).

[50] Y. Wu, S. Kolkowitz, S. Puri, and J. D. Thompson, Erasure conversion for fault-tolerant quantum computing in alkaline earth Rydberg atom arrays, (2022).

[51] C. Ryan-Anderson, J. G. Bohnet, K. Lee, D. Gresh, A. Hankin, J. P. Gaebler, D. Francois, A. Chernoguzov, D. Lucchetti, N. C. Brown, T. M. Gatterman, S. K. Halit, K. Gilmore, J. A. Gerber, B. Neyenhuis, D. Hayes, and R. P. Stutz, Realization of real-time fault-tolerant quantum error correction, Phys. Rev. X **11**, 041058 (2021).

[52] J. Hilder, D. Pijn, O. Onishchenko, A. Stahl, M. Orth, B. Lekitsch, A. Rodriguez-Blanco, M. Müller, F. Schmidt-Kaler, and U. G. Poschinger, Fault-tolerant parity readout on a shuttling-based trapped-ion quantum computer, Phys. Rev. X **12**, 011032 (2022).

[53] B. Koczor, S. Endo, T. Jones, Y. Matsuzaki, and S. C. Benjamin, Variational-state quantum metrology, New J. Phys. **22**, 083038 (2020).

[54] C. Roos, M. Chwalla, K. Kim, M. Riebe, and R. Blatt, 'Designer atoms' for quantum metrology, Nature **443**, 316 (2006).

[55] I. L. Chuang and M. A. Nielsen, Prescription for experimental determination of the dynamics of a quantum black box, J. Mod. Opt. **44**, 2455 (1997).

[56] Z. Hradil, Quantum-state estimation, Phys. Rev. A **55**, R1561 (1997).

[57] D. F. V. James, P. G. Kwiat, W. J. Munro, and A. G. White, Measurement of qubits, Phys. Rev. A **64**, 052312 (2001).

[58] T. O. Maciel, R. O. Vianna, R. S. Sarthour, and I. S. Oliveira, Quantum process tomography with informational incomplete data of two J-coupled heterogeneous spins relaxation in a time window much greater than T_1, New J. Phys. **17**, 113012 (2015).

[59] I. Bongioanni, L. Sansoni, F. Sciarrino, G. Vallone, and P. Mataloni, Experimental quantum process tomography of non-trace-preserving maps, Phys. Rev. A **82**, 042307 (2010).

[60] M.-D. Choi, Completely positive linear maps on complex matrices, Linear Algebra Appl. **10**, 285 (1975).

[61] Christopher J. Wood, Ph.D. thesis, UWSpace, 2015.

[62] P. Schindler, D. Nigg, T. Monz, J. T. Barreiro, E. Martinez, S. X. Wang, S. Quint, M. F. Brandl, V. Nebendahl, C. F. Roos, M. Chwalla, M. Hennrich, and R. Blatt, A quantum information processor with trapped ions, New J. Phys. **15**, 123012 (2013).

[63] K. Mølmer and A. Sørensen, Multiparticle Entanglement of Hot Trapped Ions, Phys. Rev. Lett. **82**, 1835 (1999).

[64] M. Ringbauer, M. Meth, L. Postler, R. Stricker, R. Blatt, P. Schindler, and T. Monz, A universal qudit quantum processor with trapped ions, arXiv:2109.06903 [quant-ph] (2021).

[65] A. Kreuter, C. Becher, G. P. T. Lancaster, A. B. Mundt, C. Russo, H. Häffner, C. Roos, J. Eschner, F. Schmidt-Kaler, and R. Blatt, Spontaneous Emission Lifetime of a Single Trapped Ca+ Ion in a High Finesse Cavity, Phys. Rev. Lett. **92**, 203002 (2004).

[66] D. Hayes, D. Stack, B. Bjork, A. C. Potter, C. H. Baldwin, and R. P. Stutz, Eliminating Leakage Errors in Hyperfine Qubits, Phys. Rev. Lett. **124**, 170501 (2020).

[67] D. Nigg, M. Müller, E. A. Martinez, P. Schindler, M. Hennrich, T. Monz, M. A. Martin-Delgado, and R. Blatt, Quantum computations on a topologically encoded qubit, Science **345**, 302 (2014).

[68] D. Niemietz, P. Farrera, S. Langenfeld, and G. Rempe, Nondestructive detection of photonic qubits, Nature **591**, 570 (2021).

[69] B. M. Varbanov, F. Battistel, B. M. Tarasinski, V. P. Ostroukh, T. E. O'Brien, L. DiCarlo, and B. M. Terhal, Leakage detection for a transmon-based surface code, Npj Quantum Inf. **6**, 102 (2020).

[70] J. Vala, K. B. Whaley, and D. S. Weiss, Quantum error correction of a qubit loss in an addressable atomic system, Phys. Rev. A **72**, 052318 (2005).

[71] M. Grassl, T. Beth, and T. Pellizzari, Codes for the quantum erasure channel, Phys. Rev. A **56**, 33 (1997).

[72] M. A. Nielsen and I. L. Chuang, *Quantum Computation and Quantum Information: 10th Anniversary Edition* (Cambridge University Press, New York, USA, 2011), 10th ed.
[73] T. C. Ralph, A. J. F. Hayes, and A. Gilchrist, Loss-Tolerant Optical Qubits, Phys. Rev. Lett. **95**, 100501 (2005).
[74] C.-Y. Lu, W.-B. Gao, J. Zhang, X.-Q. Zhou, T. Yang, and J.-W. Pan, Experimental quantum coding against qubit loss error, Proc. Natl. Acad. Sci. U.S.A. **105**, 11050 (2008).
[75] R. Laflamme, C. Miquel, J. P. Paz, and W. H. Zurek, Perfect Quantum Error Correcting Code, Phys. Rev. Lett. **77**, 198 (1996).
[76] A. Kitaev, Fault-tolerant quantum computation by anyons, Ann. Phys. **303**, 2 (2003).
[77] H. Bombin and M. A. Martin-Delgado, Topological Quantum Distillation, Phys. Rev. Lett. **97**, 180501 (2006).
[78] H. Bombin and M. A. Martin-Delgado, Topological Computation without Braiding, Phys. Rev. Lett. **98**, 160502 (2007).
[79] E. Knill, R. Laflamme, R. Martinez, and C. Negrevergne, Benchmarking Quantum Computers: The Five-Qubit Error Correcting Code, Phys. Rev. Lett. **86**, 5811 (2001).
[80] J. Chiaverini, D. Leibfried, T. Schaetz, M. Barrett, R. Blakestad, J. Britton, W. Itano, J. Jost, E. Knill, C. Langer, R. Ozeri, and D. Wineland, Realization of quantum error correction, Nature **432**, 602 (2004).
[81] M. D. Reed, L. DiCarlo, S. E. Nigg, L. Sun, L. Frunzio, S. M. Girvin, and R. J. Schoelkopf, Realization of three-qubit quantum error correction with superconducting circuits, Nature **482**, 382 (2012).
[82] D. Ristè, S. Poletto, M. Z. Huang, A. Bruno, V. Vesterinen, O. P. Saira, and L. DiCarlo, Detecting bit-flip errors in a logical qubit using stabilizer measurements, Nat. Commun. **6**, 6983 (2015).
[83] A. M. Steane, Error Correcting Codes in Quantum Theory, Phys. Rev. Lett. **77**, 793 (1996).
[84] A. Bermudez, X. Xu, R. Nigmatullin, J. O'Gorman, V. Negnevitsky, P. Schindler, T. Monz, U. G. Poschinger, C. Hempel, J. Home, F. Schmidt-Kaler, M. Biercuk, R. Blatt, S. Benjamin, and M. Müller, Assessing the progress of trapped-ion processors towards fault-tolerant quantum computation, Phys. Rev. X **7**, 041061 (2017).
[85] A. Bermudez, X. Xu, M. Gutiérrez, S. C. Benjamin, and M. Müller, Fault-tolerant protection of near-term trapped-ion topological qubits under realistic noise sources, Phys. Rev. A **100**, 062307 (2019).
[86] M. Gutiérrez, M. Müller, and A. Bermúdez, Transversality and lattice surgery: Exploring realistic routes toward coupled logical qubits with trapped-ion quantum processors, Phys. Rev. A **99**, 022330 (2019).
[87] D. Amaro, J. Bennett, D. Vodola, and M. Müller, Analytical percolation theory for topological color codes under qubit loss, Phys. Rev. A **101**, 032317 (2020).
[88] E. Dennis, A. Kitaev, A. Landahl, and J. Preskill, Topological quantum memory, J. Math. Phys. **43**, 4452 (2002).
[89] Such a model could be refined by adopting a circuit-level description and specific compilations of the stabilizer readout into gates, based, e.g., on recently proposed flag-qubit-based stabilizer readout protocols [85,97].
[90] P. Parrado-Rodriguez, C. Ryan-Anderson, A. Bermudez, and M. Müller, Crosstalk suppression for fault-tolerant quantum error correction with trapped ions, Quantum **5**, 487 (2021).
[91] A. L. Grimsmo and S. Puri, Quantum Error Correction with the Gottesman-Kitaev-Preskill Code, PRX Quantum **2**, 020101 (2021).
[92] J. Tilly, H. Chen, S. Cao, D. Picozzi, K. Setia, Y. Li, E. Grant, L. Wossnig, I. Rungger, G. H. Booth, and J. Tennyson, The variational quantum eigensolver: A review of methods and best practices, arXiv:2111.05176 [quant-ph] (2021).
[93] C. Kokail, C. Maier, R. van Bijnen, T. Brydges, M. K. Joshi, P. Jurcevic, C. A. Muschik, P. Silvi, R. Blatt, C. F. Roos, and P. Zoller, Self-verifying variational quantum simulation of lattice models, Nature **569**, 355 (2019).
[94] S. Krinner, N. Lacroix, A. Remm, A. D. Paolo, E. Genois, C. Leroux, C. Hellings, S. Lazar, F. Swiadek, J. Herrmann, G. J. Norris, C. K. Andersen, M. Müller, A. Blais, C. Eichler, and A. Wallraff, Realizing repeated quantum error correction in a distance-three surface code, arXiv:2112.03708 [quant-ph] (2021).
[95] R. Stricker, D. Vodola, A. Erhard, L. Postler, M. Meth, M. Ringbauer, P. Schindler, R. Blatt, M. Muller, and T. Monz, Data for "Characterizing Quantum Instruments: From Nondemolition Measurements to Quantum Error Correction" (2021). https://doi.org/10.5281/zenodo.6901982.
[96] H.-R. Wei, B.-C. Ren, and F.-G. Deng, Geometric measure of quantum discord for a two-parameter class of states in a qubit–qutrit system under various dissipative channels, Quantum Inf. Process. **12**, 1109 (2013).
[97] R. Chao and B. W. Reichardt, Quantum Error Correction with Only Two Extra Qubits, Phys. Rev. Lett. **121**, 050502 (2018).